Development of Wrinkled Surface for Enhanced Light Trapping in Organic Solar Cells

Malia Steward

A thesis

submitted in partial fulfillment of the

requirements for the degree of

Master of Science in Electrical Engineering

University of Washington

2018

Committee:

Seungkeun Choi, Chair

Tadesse Ghirmai

Hrair Aintablian

Program Authorized to Offer Degree:

Engineering and Mathematics

University of Washington

Abstract

Development of Wrinkled Surface for Enhanced Light Trapping in Organic Solar Cells

Malia Steward

Chair of the Supervisory Committee:
Dr. Seungkeun Choi
Engineering and Mathematics

There have been great interest in organic photovoltaics (OPVs) due to their potential for the development of low-cost, high throughput, and large-area solar cells with a flexible form factor. Hence, the power conversion efficiency of OPVs has been dramatically improved for the past two decades. Although the power conversion efficiency (PCE) of OPVs exceeds 10% now, the PCE of thin-film based solar cells is fundamentally limited by the ability of the photo-active layer to absorb the incident sunlight. The external quantum efficiency (EQE) is used to describe this ability and rarely exceeds 70% for the state-of-the-art OPVs, implying that only 70% of incident photons contributes to a photo-current generation. The EQE can be improved by trapping more light in the active layer which is very challenging for thin-film based photovoltaics.

In this research, I have investigated optimization of the organic solar cell fabrication by tuning a charge carrier transport layer and also developed a new metallization method in order to replace vacuum deposited silver electrode with electroplated copper which is less expensive and better fits to the industry manufacturing. I also investigated a number of methods to fabricate optimum wrinkle structure that can be used as a light trapping vehicle for organic solar cells. I fabricated wrinkles on SU-8 polymer by controlling the softness of SU-8. While wrinkles generally

produced after metal deposition, I found that a more suitable wrinkle profile can be fabricated before the metal deposition. Future work will focus on the development of reproducible, scalable, and high throughput wrinkle fabrication with an optimum profile and the demonstration of highly efficient organic solar cells by enhancing light trapping thanks to the wrinkles.

TABLE OF CONTENTS

LIST OF FIGURES

LIST OF TABLES

LIST OF SYMBOLS AND ABBREVIATIONS

BHJ	Bulk Heterojunction
CTE	Coefficient Thermal Expansion
$CuSO_4$-$5H_2O$	Cupric sulfate
DI	Deionize
EHP	Electron Hole Pair
ETL	Electron Transport Layer
EQE	External Quantum Efficiency
FF	Fill Factor
HTL	Hole Transport Layer
ITO	Indium-Tin Oxide
J_{SC}	Short Circuit Current Density
MLA	Microlens Array
MoO_3	Molybdenum Trioxide
MSL	Micro-structured Scattering Layer
N_2	Nitrogen
OPV	Organic Photovoltaic
OSC	Organic Solar Cell
P3HT	Poly(3-hexylthiophene-2,5-diyl) regioregular
PCBM	Phenyl-C_{61}-butyric acid methyl ester
PCE (η)	Power Conversion Efficiency
PDMS	Polydimethylsiloxane
PEIE	Polyethylenimine Ethoxylated
SNL	Silica Nanoparticle Layer
SPP	Surface Plasmon Polariton
H_2SO_4	Sulfuric acid
TCFE	Transparent Conductive Front Electrode
V_{OC}	Open Circuit Voltage
WF	Work Function
ZnO	Zinc oxide

ACKNOWLEDGEMENTS

Foremost, it is with immense gratitude that I acknowledge my advisor, Dr. Seungkeun Choi for his continuous support, patience, motivation, advising, and guiding me throughout the process of my Master Thesis study and related research. Besides my advisor, I would like to thank the rest of my thesis committee: Dr. Tadesse Ghirmai, and Dr. Hrair Aintablian for their encouragement, insightful comments, and thoughtful questions.

Finally, I must express my profound gratitude to my mother for providing me with unfailing support and continuous encouragement throughout my years of study.

DEDICATION

I dedicate my Thesis to the memory of my late father, Charles Evans Steward. Thank you for being there for me, your spiritual guidance, kindness, devotion, and your endless love. Your continuous encouragement and support helped me pursue my educational ambitions which helped shape who I am today. You will always be in my heart and memories.

Chapter 1

INTRODUCTION

The impact of developing viable alternative energy sources is an immense undertaking. Despite their long history starting from the Industrial Revolution, fossil fuels, such as petroleum, natural gas, and coal, are still used as the main energy source in modern society. For U.S. alone, fossil fuels made up 81.5% of total U.S energy consumption in 2015 and is still expected to increase by 13.4% and 5.4%, for natural gas and coal consumption, respectively, by year 2040, according to U.S. Energy Information Administration (EIA) [1]. Consequently, the indiscriminate use of fossil fuels is expected to cause serious global problems, such as an energy crisis induced by resource depletion and environmental pollution. Accepting the fact that we are depleting our fossil fuel sources, it is of great interest to develop methods that mitigate disturbances in our environment that reduce factors that create climate change and global warming. To replace fossil fuels and overcome these global issues, the development of renewable energy sources, such as biomass, geothermal or wind power, and solar energy, is becoming an important factor for protecting the environment.

Photovoltaic (PV) technologies, which directly absorb photons from sunlight and convert them into electricity without producing any harmful effects, have been emerging as sustainable and environmentally friendly energy sources. Photovoltaics have very diverse applications in industry as well as in consumer market, as shown in Fig. 1. Some of the applications are highly unique, such as satellites and portable chargers. For example, Vanguard I (Fig.1 (a)), designed by the U.S. Naval Research Laboratory (NRL), was the world's first solar-powered satellite launched in 1958, to gather environmental data, such as geodetic measurements [2]. An additional historical example includes Solar Impulse 2 (Fig.1 (b)), the first solar-powered airplane to tour the globe in

nearly 17 months, covering 14,000 km with more than 17,000 solar cells on its wings [3]. Other groundbreaking examples can range from large-scale to small-scale products, including Germany's Waldopolenze Solar Park (Fig.1 (c)), one of the many largest thin-film solar cell farms [4], and a solar rooftop of the building of National Renewable Energy Laboratory (NREL) (Fig.1 (d)), to a portable solar charger that is lightweight and waterproof from Wildtek products (Fig.1 (e)) [5].

Using various photoactive semiconductors, there has been intense research effort into the development of cost-efficient photovoltaic technologies. As a prospective solar technology,

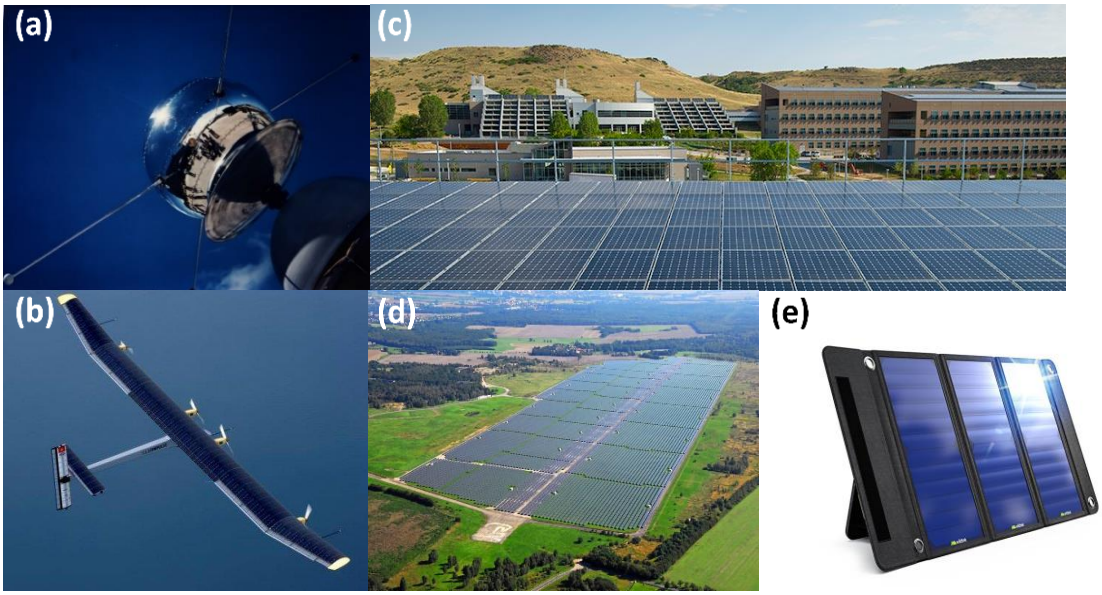

Figure 1. Applications of renewable energy resources. (a) Vanguard I satellite with solar cells, (b) Solar impulse 2 with solar cells designed on the pane wings, (c) NREL building with rooftop solar panel rooftop, (d) Waldopolenze Solar Park in Leipzig, Germany, (e) Wildtek waterproof portable solar charger.

organic photovoltaics (OPV) have attracted considerable attention due to their advantageous features compared to the rigid and fragile inorganic-based solar cells, such as light-weight, flexibility, wearability, biocompatibility, printability, and easy integration on curved surfaces. Therefore, organic solar cells (OSC) are expected to become promising fossil-fuel alternatives that

are inexpensively available, not only in advanced countries but also in poor and developing countries. Altogether, solar cells have proved to be dependable and ultimately reliable in various forms of application, becoming an intricate part in the renewable energy sector, and continuing to make significant developments in today's technology. For this reason, the potential of solar energy is beyond what can be currently imagined with such innovative and creative changes that are currently underway.

Chapter 2

BACKGROUND AND MOTIVATION

2.1 Organic Photovoltaics

One of the many advantages of solar cells is that not only does it utilize the familiar, yet highly abundant element, silicon, but as well as introducing other alternatives in approaching the same goal of harvesting solar: flexible thin-film solar cells. As opposed to silicon's rigid surfaces when fabricating solar cells, we have flexible thin-film solar cells as replacements. With the use of these thin-film solar cells, solar power can even be integrated into the material of buildings. Notably, photovoltaics can be fabricated in such a way that it can be applied to curvatures of buildings, objects, or appliances, due to its flexibility.

Thin-film organic photovoltaics have been explored extensively in the last few decades as alternatives to single crystalline-based silicon solar cells due to the promising potential for the development of large-area, low-cost, light-weight solar modules with highly flexible form factors. In organic solar cells, organic light-absorbing active layers are sandwiched between two electrodes with a bulk heterojunction where donor and acceptor materials are intermixed [6].

Solar cells are tested in the dark and under the illumination to characterize their electrical performance. A graph of current density versus voltage (J-V) is commonly used to illustrate the characteristics of solar cells, as shown in Fig. 2. When the device is measured in the dark, the J-V curve passes through the origin with no potential or current flow (grey curve). However, when exposed to light, the J-V curve shifts downward, as illustrated in Fig. 2 (red curve) due to the photogenerated current. The following photovoltaic parameters are commonly used to describe the characteristics of solar cells:

1. **Short-Circuit Current Density, J_{SC}**

   The current flow through a solar cell under illumination when two terminals are shorted (hence, "short-circuit") is defined as the short-circuit current density. The short-circuit current density is the maximum current density the solar cell can produce by shorting its terminals, without generating any power since the voltage is zero, i.e., short-circuit.

2. **Open-Circuit Voltage, V_{OC}**

   Open-circuit voltage is the voltage across the solar cell under illumination when no current is flowing. This is the maximum possible voltage across a photovoltaic cell when the solar cell is an open circuit, thus generating no power.

3. **Maximum power output, P_{max}**

   Solar cells generate power in the 4th quadrant only, as shown in Fig. 2. Current density and voltage at the maximum power generation point are defined as J_{max} and V_{max}.

4. **Fill Factor, FF**

   Fill factor is the ratio of the solar cell's actual maximum power output ($P_{max} = J_{max} \times V_{max}$) to ideal power output ($P_{ideal} = J_{SC} \times V_{OC}$), represented by the formula:

$$FF = \frac{P_{max}}{P_{ideal}} = \frac{J_{max} \times V_{max}}{J_{sc} \times V_{oc}} \quad (1)$$

   The FF is a critical parameter used to measure how well the photogenerated charge carriers can be extracted from solar cells [7]. Hence, solar cells with a higher fill factor exhibit more "squareness" in their J-V curve.

5. Power Conversion Efficiency (PCE or η)

Power conversion efficiency is defined as the ratio of maximum power output (P_{max}) to optical power input ($P_{optical\ input}$). It is a measure of the amount of power produced by a solar cell in relation to the power available in the incident solar radiation (P_{max}) yielding the formula:

$$PCE, \eta\ (\%) = \frac{P_{max}}{P_{optical\ input}} = FF\ \frac{J_{SC} \times V_{OC}}{P_{optical\ input}} \tag{2}$$

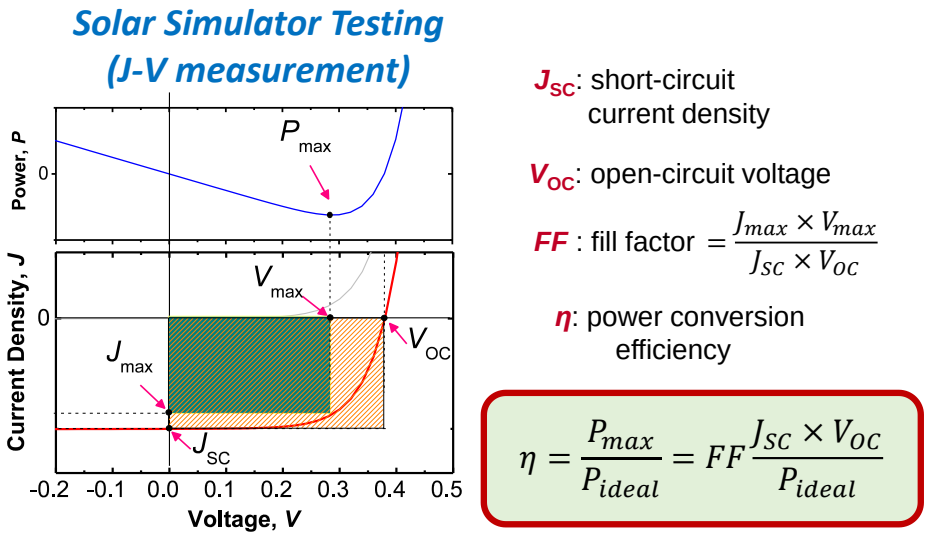

Figure 2. OPV parameters calculation for short-circuit current density (J_{SC}), open-circuit voltage (V_{OC}), fill factor (FF), and power conversion efficiency (η).

Solar cells are composed of many layers of materials including a semiconducting active layer that converts energy from the suns' rays to electricity. When the suns' rays hit the solar cell, the electron-hole pairs (EHPs) are immediately generated in the active layers. Once EHPs are generated, they are separated and transported to the corresponding electrodes assisted by transporting layers. Therefore, there must be efficient extraction of electrons and holes within the

active layer to ensure sufficient current flow. In addition, it is very important to have a good absorption as it directly relates to J_{sc}. In fact, efficiency of thin-film based solar cells is critically limited by poor light absorption [7-10].

Active layer thickness of a solar cell is very important to obtain a high PCE and FF. For example, a thicker active layer is required for enough light absorptions, thereby increasing J_{SC}. However, too thick of an active layer limits effective extraction of charge carriers, thereby decreasing FF [7]. The optimum active layer thickness for efficient charge separation, based on organic semiconductors (polymer and fullerene derivatives), is found to be ~100 nm [6]. However, at this thickness, a considerable portion of the incoming light is not absorbed.

2.2 Light Trapping Scheme

One way to improve light absorption within the active layer thickness is to adopt light trapping schemes in which the path length of photons inside the active layer is maximized once photons enter the layer. Increased path length increases the probability of absorption of photons and results in increased photo-current generation per incident photon. In general, the light-trapping effect follows either the wave-optical regime (feature size comparable to wavelength) or the ray-optical regime (feature size much larger than wavelength), as shown in Fig. 3. Compared to these wave-optical schemes, ray-optical light-trapping regimes offer a number of advantages due to the much larger feature size compared to the wavelength: broadband absorption enhancement, less

dependence on the incident light angles, and undisturbed morphologies of the active layer. However, ray-optics-based light trapping has rarely been employed for thin-film organic solar cells

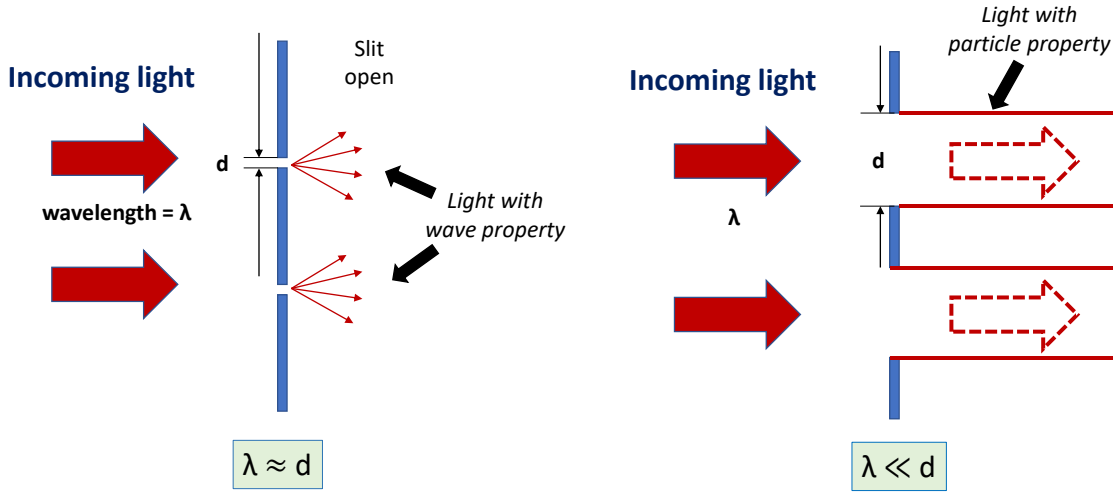

Figure 3. Optical design differences between (a) wave-based optics (slit opening is comparable to light wavelength, exhibiting wave-like behavior which depend on light wavelength itself), and (b) ray-based optics (slit opening is much larger than the light wavelength, exhibiting particle-like behaviors, ray-optic).

due to multiple engineering challenges. Therefore, this research investigates an optimum design for ray-optics-based 3-D light-trapping structures and develops fabrication processes to overcome the technical challenges.

2.2.1 Wave Optics-Based Light Trapping by Nanopatterns

Light-trapping schemes using wave-optical regimes are dominant and typically utilize nanoscale features, like textures between the thin-film layers [11, 12], metallic- or dielectric-nanostructures [13, 14], or an array of micro-lens structures [15]. For thin films, examples include textured surfaces and photonic crystals. For instance, Wang et al. demonstrated a textured SiO_2 antireflective layer by performing reactive ion etching (RIE) process (Fig. 4(a)) [11]. This method was applied for an organic solar cell, which resulted in a 5% efficiency

improvement due to light trapping enhancement. An additional example includes a randomly textured surface and photonic crystals demonstrated by Wiesendanger et al. Through design and simulation, the authors demonstrated how a photonic structure can naturally grow on the random textured surface [12]. This photonic structure would transition from amorphous to a periodic structure, thereby sustaining the largest absorption enhancement for light trapping mechanism. For metallic- or dielectric- nanostructures, Liu et al. fabricated a periodically-textured ZnO Transparent Conductive Front Electrode (TCFE) with broadband light trapping properties. This method utilized a self-assembled polystyrene (PS) sphere, where the textured ZnO TCFE was later fabricated on top (Fig. 4(b)) [14].

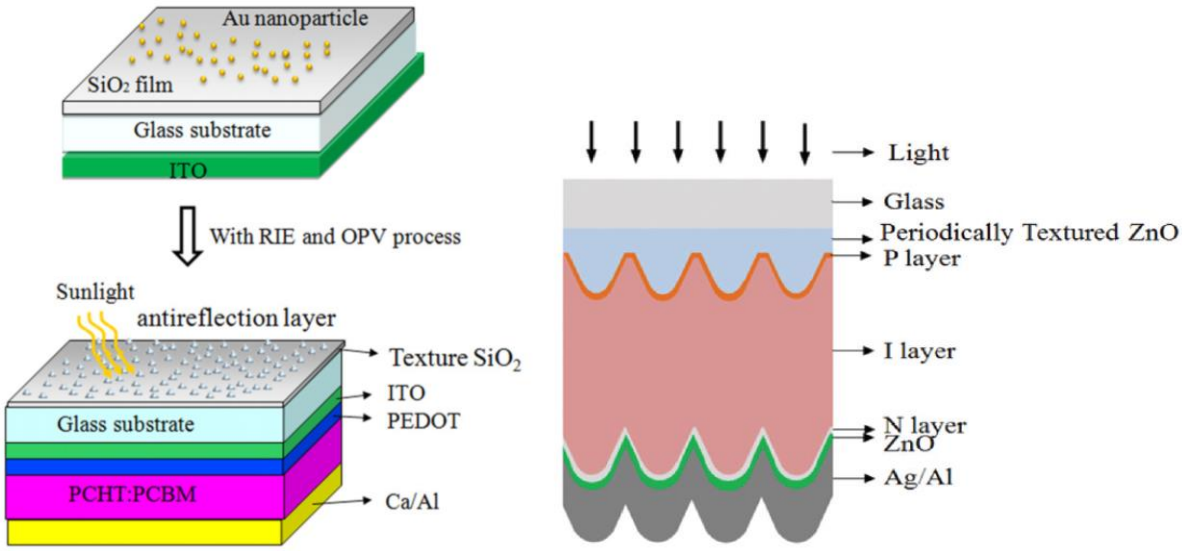

(a) (b)

Figure 4. Examples of wave-optical regimes. (a) Fabrication of producing a textured SiO2 layer by reactive ion etching (ROE), and making an OPV [11], (b) Schematic diagram of solar cell with periodically double-layered HCO/AZO transparent conductive front electrodes [14].

Atwater et al. investigated how plasmonic structures can aide in improving photovoltaic devices. Light scattering using particle plasmonic and surface plasmon polaritons (SPP) are two main types of plasmonic structures that can be utilized (Fig. 5(a)) [13]. As for micro-lens structures, Tvingstedt et al. demonstrated an array of micro-lens in conjunction with self-aligned array of micro-apertures located in the highly reflecting mirror (Fig. 5(b)). This method allows the reflected photons to be recycled, rather than being lost, within the photoactive layer, giving the potential to be employed in thinner films [15].

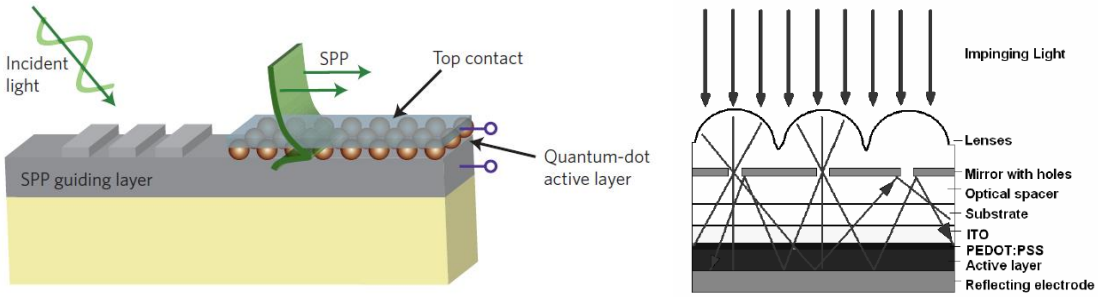

(a) (b)

Figure 5. Examples of wave-optical regimes. (a) Plasmonic quantum-dot solar cell designed for enhanced photo-absorption in ultrathin quantum-dot layers mediated by coupling surface plasmon polaritons (SPP) [13]. (b) schematic and operational principle of microlens in a solar cell [15].

Despite the many advantages and potentials wave-optics regime can deliver, these approaches do suffer from the following shortcomings: (1) a high chance of electrical defects due to the size of the nanostructures compared to the active layer thickness, (2) dependence on the incident light angles, and/or (3) narrowband spectrum [16]. The above wave-optics regimes and its examples are summarized in Table 1.

Table 1. Summary of wave optical regime examples and applications

Author	Wave-Optics Application	Method	Fabrication of Optical Regime
Wang et al. [11]	Thin film	Textured SiO_2 film	Reactive ion etching (REI)
Wiesendanger et al. [12]	Thin film	Randomly textured surface and photonic crystal	Photonic structure naturally grown on randomly textured surface
Atwater et al. [13]	Metallic, dielectric nanostructures	Plasmonic structures	Particle plasmonic and surface plasmon polaritons (SPP)
Liu et al. [14]	Metallic, dielectric nanostructures	Periodically-textured ZnO transparent conductive front electrode (TCFE)	Self-assembled polystyrene (PS) spheres
Tvingstedt et al. [15]	Microlens	Array of micro lens with self-aligned array of micro-apertures via highly reflecting mirror	Master mold comprised of an array of inverted (concave) lens

2.2.2 Ray Optics-Based Light Trapping by Using Textured Surface

For ray optics regime, the feature sizes are much larger than the incident wavelengths, promoting enhancement of absorption in the infrared part of the spectrum [17]. Simple geometric structures contribute to light absorption enhancement due to an increased optical path inside the photoactive material, which is achieved by exploiting total internal reflection [18, 19]. One way to utilize ray-optical light trapping for organic solar cells is to fold two planar solar cells to create a V shape (Fig. 6(a)) [8, 20-22], or a cone shape (Fig. 6(b)) [23], which were demonstrated by Zhou et al., and Zhen et al., respectively. Due to the multiple bounces of unabsorbed light in this V-shape

geometry, the total optical path length within the active layers of the two individual cells is increased and absorption is highly enhanced [16]. The V-shape configuration combines spectral broadening and light trapping, thus enhancing optical absorption and increasing photocurrent generation, which results in an increased power conversion efficiency.

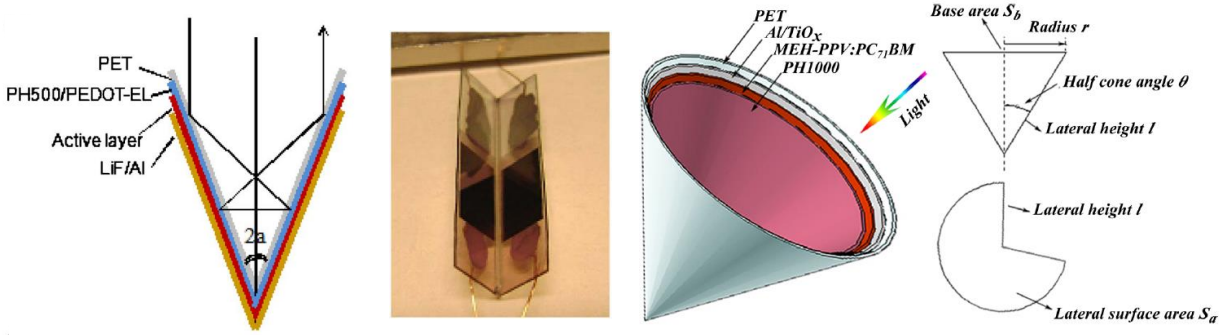

(a) (b)

Figure 6. Geometric-based light trapping structures utilizing ray optics for solar cells using (a) a folded V-shape [22] and (b) cone shape [23].

A more advanced approach, developed by Tvingstedt et al, utilized the same V-shape method, however, utilized two different photoactive materials of different bandgaps, in a folded reflective tandem polymer solar cell where all the reflected lights of the first solar cell is directed to the next solar cell, as shown in Fig.7. With a combination of a photoactive layer with a high bandgap and a photoactive layer with a low bandgap, optical reflectance from the combined cells in a folded configuration demonstrates broadening of optical absorption, and the overall absorptance is strongly influenced by the fold angle [20]. Such techniques as the V-shape configuration produce greater than 50% increase in power conversion efficiency simply by folding two identical planar cells [21, 22]. As for the cone shape, there is multi-absorption in all 360 degrees direction, where small angles produce effective light trapping due to reabsorption within the photoactive layer in all directions [23]. A summary of the ray-optic regimes and its examples are in Table 2.

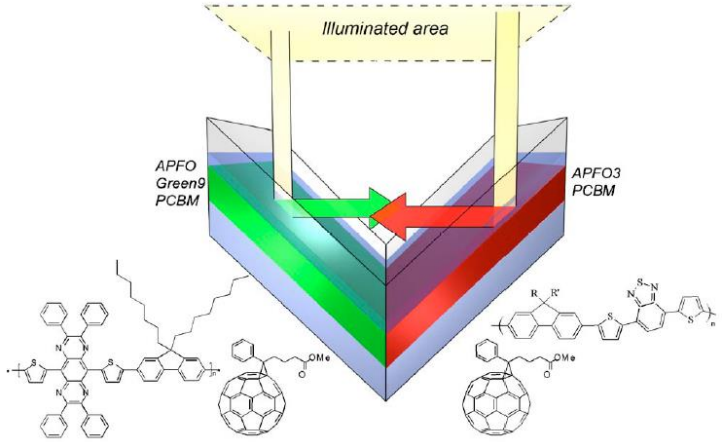

Figure 7. Folded tandem solar cell using two different photoactive layers of different bandgaps: APFO-Green9:PCBM and APFO3:PCBM [20].

Table 2. Summary of ray optical regime examples and applications

Author	Ray-Optics Application	Method	Fabrication of Optical Regime
Kim et al. [8]	Polymer solar cell	Folded in V-shape configuration	Two planar devices with PCDTBT:PCBM photoactive layer are attached at a V-shape angle
Tvingstedt et al. [15]	Polymer solar cell	Folded in V-shape configuration	Two photoactive layers of different bandgaps are folded to face each other
Zhou et al. [22]	Thin film & Polymer solar cell	Folded in V-shape configuration	Two planar devices with APFO-3:PCBM photoactive layer folded
Zhen et al. [23]	Polymer solar cell	Rolling in a cone shape configuration	Compressive stress (folding) of an inverted ITO-free structure
Cho et al. [24]	Thin film & Polymer solar cell	Folded in V-shape configuration	Two planar devices are folded to face each other

Based on Table 2, it is observed that simple geometrical structures are used to enhance light trapping and light absorption compared to the complex, typically nanoscale structures, of wave-optical regimes. For this reason, utilizing ray-optical light trapping regimes works for a broadband spectrum rather than a specific narrowband spectrum, due to the thickness of the photoactive layer, which are typically present in bulk heterojunction (BHJ) organic solar cells [25].

2.3 Motivation and Thesis Outline

The purpose of this research is to demonstrate highly efficient organic solar cells by employing light trapping structure in ray-optics regime. The body of the thesis is comprised of two chapters. Chapter 3 summarizes the research that has been done in organic solar cell optimization and wrinkle generation for an enhanced light trapping. Sections 3.1.1 and 3.1.2 highlight the differences between a conventional and inverted organic solar cell structure and how each layer contributes to converting solar energy to power. Section 3.1.3 describes how to find optimum thin film thickness experimentally and section 3.1.4 discusses how to expedite commercialization of organic solar cell technology by replacing vacuum deposited silver electrode with electroplated copper. Sections 3.2.1 and 3.2.2 describe the basics of wrinkle generation and characterization. Section 3.2.3 presents experimental details of the wrinkle generation optimized for organic solar cell application. Lastly, Chapter 4 includes conclusions and future work detailing the integration of light trapping with an organic solar cell.

Chapter 3

DESIGNS, METHODS, AND IMPLEMENTATION

3.1 Optimization of Organic Photovoltaics (OPV)

This section discusses the physical layout and fabrication process of OPV, their performance, and analysis of each stated material that contributes to the conversion of the power efficiency. This section primarily focuses on the importance of transporting layers that facilitates charge carriers, and a novel metallization method of an OPV. All OPV structures follow an inverted architecture rather than a conventional design. Based on the outcomes of this chapter, highly efficient and low cost OPV due to the electroplated top electrode will be fabricated on top of wrinkled surface in order to enhance light trapping.

3.1.1 Organic Solar Cell Architecture: Conventional vs. Inverted

A typical OPV is composed of a layer of organic semiconductor sandwiched between two electrodes, the anode and cathode, usually fabricated on a glass substrate. One of the electrodes must be transparent so that light can be absorbed by organic semiconductors. What makes this technology so promising is that there are a number of ways that organic semiconductor can be coated with a simple, inexpensive, and high throughput methods such as spin-coating, spray coating, and roll-to-roll processing. OPVs can also be designed in two different structures: conventional structure, and inverted structure, as shown in Fig. 8. Based on the stated architecture description, the placement of the anode and cathode determines the appropriate structure [26]. Both structures consist of a top and bottom electrode. Conventional OPVs have the anode as the bottom electrode, and cathode as the top electrode (Fig.8 (a)) while inverted OPVs have the anode as the top electrode, and cathode as the bottom electrode (Fig.8 (b)) [26].

Typically, for conventional OPVs, a low work-function (WF) metal, such as Aluminum (Al), Calcium (Ca), or Barium (Ba), is used as a cathode while a high WF transparent conducting metal oxide, such as Indium-Tin Oxide (ITO) or Fluorine doped Tin Oxide (FTO) is used as an anode [26-29]. However, other research work had demonstrated how conventional OPVs result in poor device performance and low device stability due to the degradation of the low WF cathode metal [29]. This also limits exposure time in ambient air when being handled and processed since oxygen and moisture can be diffused into the polymer layer through the top metal electrode [28]. Therefore, an inverted structure has been developed in order to overcome these challenges [30]. ITO or FTO is now used as a cathode, and a high WF metal, such as Gold (Au), Silver (Ag), and Copper (Cu), is used as the anode [30, 31]. Therefore, this device structure allows more stability in ambient air due to high work function metals, thus sustaining the efficiency longer period time without degradation [31]. As a result, this makes inverted structures highly attractive for commercialization [32, 33].

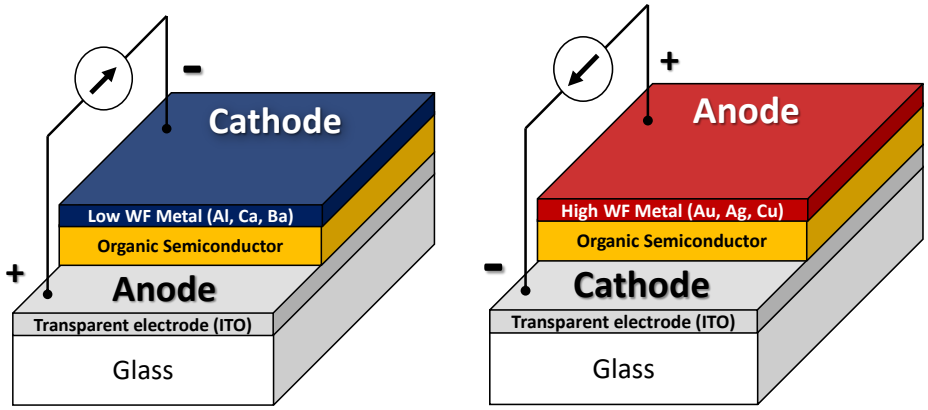

(a) (b)

Figure 8. Device architecture of an organic solar cell showing (a) conventional structure, and (b) inverted structure.

3.1.2 Role of Each Layer in Organic Solar Cells

In this research, I developed an inverted organic solar cell based on Indium-tin oxide (ITO)/ Zinc oxide (ZnO)/ poly(3-hexylthiophene) (P3HT): PCBM/(Molybdenum oxide) MoO_3/(Silver) Ag, as shown in Fig. 9. Creating a solar cell involves a strategic fabrication process that consists of several layers which must be optimized in terms of thickness, morphology, and materials for a highly efficient organic solar cell [32, 34-39]. P3HT:PCBM creates bulk heterojunctions (BHJs) of donors and acceptors that absorb sunlight and create bonded electrons and holes, also known excitons. ITO and Ag serves as the electrodes, collecting electrons and holes, respectively. The remaining two layers, ZnO, and MoO_3, facilitate transport of electrons and holes toward ITO and Ag electrode and are known as the electron transporting layer (ETL), and the hole transporting layer (HTL), respectively.

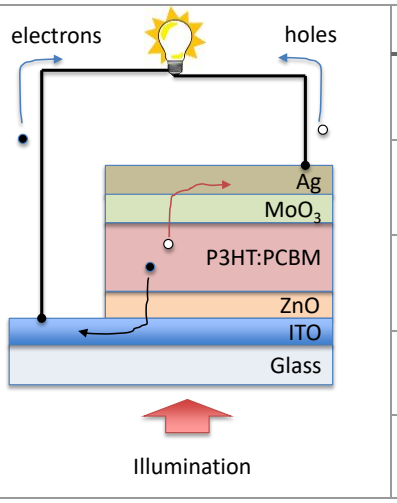

Material	Description
Ag	Opaque electrode **(Anode, +)**
MoO_3	Hole transport layer (HTL)
P3HT:PCBM	Active layer that produces holes and electrons
ZnO	Electron transport layer (ETL)
ITO	Transparent electrode **(Cathode, -)**

Figure 9. Light is absorbed by P3HT:PCBM and generated charge carriers are transported via ZnO and MoO_3 layers toward collecting electrodes.

While there are many reports on the optimization of active layer and ETL which are very reproducible due to the nature of spin coating method, quality of the thermally evaporated MoO_3 strongly depends on process parameters such as the vacuum, deposition rate, and equipment.

Hence, I optimized MoO_3 process parameters such as thickness and deposition rate for this research.

3.1.3 Optimization of the Hole Transport Layer

Fabricating solar cells start with an ITO-coated bottom electrode glass slide, followed by ZnO, an ETL, created with 1.00g zinc acetate dihydrate, 0.280g ethanolamine, and 10.0mL 2-methoxyethanol, spin-coated at 2000rpm for 60 sec. ZnO is then annealed at 200˚C for 1 hour. The active layer of poly(3-hexylthiophene) (P3HT): PCBM (1:0.7, weight ratio) was spin-coated at 3500 rpm for 8 sec. in the N_2-filled glove box from a dichlorobenzene solution (60 mg/ml), followed by setting the samples for 40 minutes in an enclosed petri dish to promote solvent annealing process. Then, the samples were annealed on a hotplate at 110°C for 10 min. The device was then transferred to a thermal evaporator and 15 nm, 20 nm, and 25 nm of MoO_3 and 150 nm of Ag top-electrodes were deposited through a shadow mask under high vacuum. Completing the solar cell with the top electrode completes the circuit, as seen in Figures 10 and 11. Electron charge

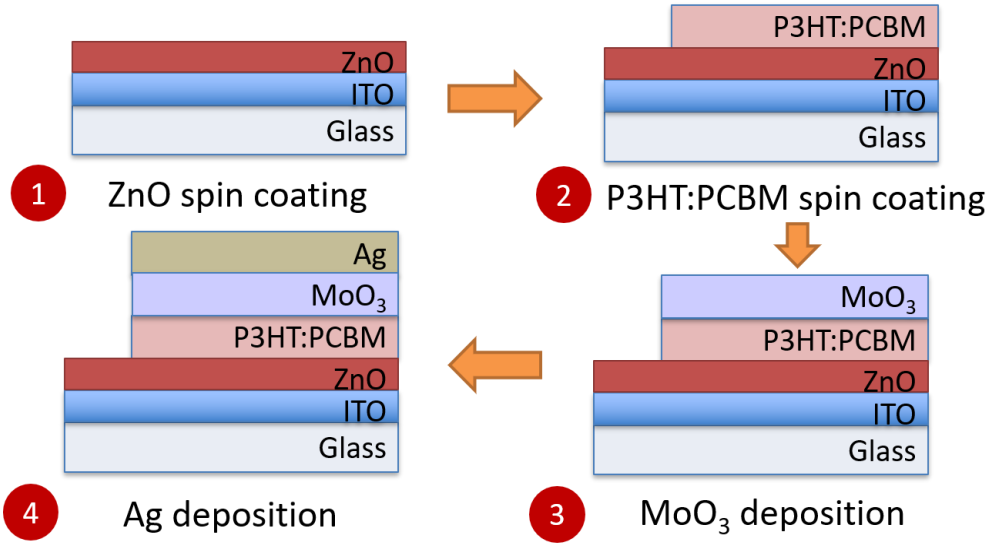

Figure 10. Design and fabrication process of a complete organic solar cell showing (1) ZnO spin coating, (2) P3HT:PCBM spin coating, (3) MoO_3 deposition, and (4) Ag deposition.

carriers transport through ZnO to ITO, while the hole charge carriers transport through MoO_3 to Ag. This experiment addresses the optimized thickness of the HTL, MoO_3, to further improve the PCE. In focusing on MoO_3, results determined that as the layer thickness of MoO_3 reduces, the PCE increases. In opposition, as the layer thickness of MoO_3 increases, the PCE decreases. By controlling the thickness of the hole transport layer, an optimized thickness can be determined to produce high PCEs.

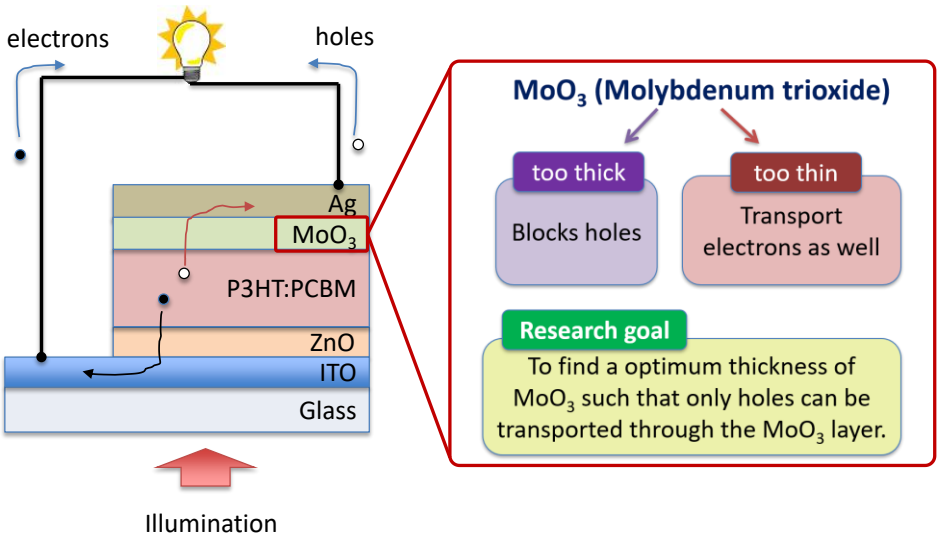

Figure 11. Architecture of an inverted OPV with hole transport layer, MoO_3, and its thickness description.

Without proper separation of electrons and holes via optimized ETL and HTL materials and thickness, solar cells will not efficiently extract generated electric charges. This research, therefore, focuses on the optimization of HTL. Thermally deposited MoO_3 in a high vacuum is used as an HTL and its thickness plays a key role for the solar cell performance. For example, having too thin of the layer will also transport electron charge carriers while having too thick of the layer will block the hole charge carriers; both causing insufficient and drastically low PCE. Efficiency results are shown in Table 3. In our experiment, the PCE decreases by 16% as the layer thickness of MoO_3 increases from 15nm to 25nm. By optimizing this HTL thickness, highly

efficient organic solar cells can be demonstrated based on the device structure shown in the Fig. 11. Therefore, this research demonstrates the importance of process optimization for a highly efficient organic solar cell.

This experiment was developed at the UWBB 226 research lab where all the necessary equipment is housed. A well-established microfabrication technology is used to create patterned ITO layer and ZnO layer in a cleanroom while organic semiconductors (P3HT:PCBM with di-chlorobenzene (DCB)) are spin-coated inside a nitrogen-filled glove box. MoO_3 and Ag are thermally deposited in a high vacuum thermal evaporator. An Oriel solar simulator was used to measure the PCE (P_{solar} = 100 mW/cm^2). Current density and voltage (J-V) curves were measured with Keithley 2400 source meter with a 4-point measurement method.

Table 3. Summary of organic solar cells with different MoO_3 thickness and process parameters.

Fabricated OPVs		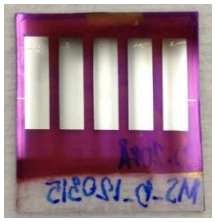	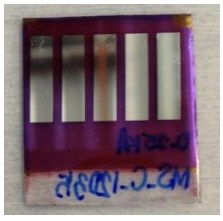
MoO_3 Thickness	15 nm	20 nm	25 nm
Efficiency (%)	2.5 ± 0.3	2.3 ± 0.1	2.1 ± 0.3
Pressure (Torr)	2.5×10^{-6}	2.5×10^{-6}	2.5×10^{-6}
Deposition Rate (Å/s)	0.2	0.2	0.2

**** Statistics based – 5 devices per sample***

3.1.4 Copper-Plated Top Electrode for an Inverted Organic Photovoltaic

There has been tremendous interest in new metallization strategies in silicon photovoltaics mainly driven by the increasing silver prices and reduced silicon wafer thicknesses [40]. In silicon photovoltaic technology, industry attractive screen-printing technology has been

widely used to coat silver electrode followed by a light induced plating (LIP) of Copper (Cu) in order to improve the conductance of silver (Ag) [41]. Therefore, very little Ag is required as a seed layer, hence, decreasing materials cost significantly. Incorporating this emerging metallization method with a light-trapping enhanced OPV is not only essential for realizing greater efficiency, but as well as being more industry-friendly, bringing this realization one step closer to commercialization [42].

However, in OPVs, application of electroplating process has been limited to the bottom electrode of ITO as the ITO significantly limits the performance of large-area OPV due to its lower conductivity, typically an order of two lower, compared to the opaque top electrodes such as Ag or Aluminum (Al) [43]. However, increased cost of silver also hurdles the large-scale deployment of OPV and reports with this important issue for the OPV are relatively scarce. Particularly, it is difficult to apply an electroplating process to the completed OPV device because of the sensitivity of organic semiconductors to the acids and water. Therefore, in this work, I reported an improved performance of OPV by electroplating Cu on top of Ag electrode as a top electrode. 30 nm of Ag was used a s a top electrode and 200 nm of Cu was electroplated, showing improved FF and PCE by 35% and 25%, respectively.

Similarly, to the fabrication process in Section 3.1.3 (Optimization of the Hole Transport Layer), inverted organic solar cells were fabricated on 1" × 1" glass substrates coated with ITO, which acts as a transparent bottom electrode (cathode). An active area of 0.3 cm^2 was created by patterning the ITO using photolithography and chemical wet etching. Then, the ITO was cleaned in sequential ultrasonic baths of acetone and isopropanol for 20 minutes each, followed by drying in the oven for 30 minutes. Polyethylenimine ethoxylated (PEIE) was spin-coated, from a 0.4 wt% solution mixed with 2-methoxyethanol, at 5000 rpm for 60 sec. The active layer of poly(3-

hexylthiophene) (P3HT): PCBM (1:0.7, weight ratio) was spin-coated at 3500 rpm for 8 sec. in the N_2-filled glove box from a dichlorobenzene solution (60 mg/ml), followed by setting the samples for 40 minutes in an enclosed petri dish to promote solvent annealing process. Then, the samples were annealed on a hotplate at 120 °C for 10 min. The device was transferred to a thermal evaporator and 10 nm of MoO_3 and 30 nm of Ag top-electrodes were deposited through a shadow mask under high vacuum. The completed device had an active area of 0.3 cm^2 and an inverted OPV structure of Glass/ITO/PEIE/P3HT:PCBM/MoO_3/Ag, as shown in Figure 12.

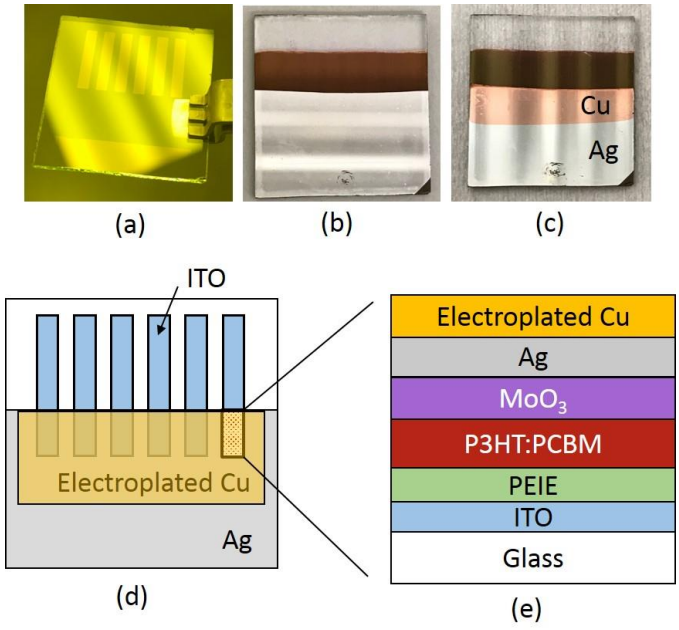

Figure 12. Inverted OPV device structure: (a) ITO patterns, (b) before Cu plating, (c) after Cu plating, (d) layout, and (e) cross-sectional structure.

Copper plating solution was prepared by mixing 250 mg cupric sulfate ($CuSO_4$-$5H_2O$) and 25 ml sulfuric acid (H_2SO_4) in 1 liter of deionized water. 200nm of copper was electroplated by applying a dc current density of 10 mA/cm^2, as shown in Fig. 13. Photoactive areas were completely submerged in the solution bath during the copper plating. After plating, the devices were rinsed with DI water and dried with N_2.

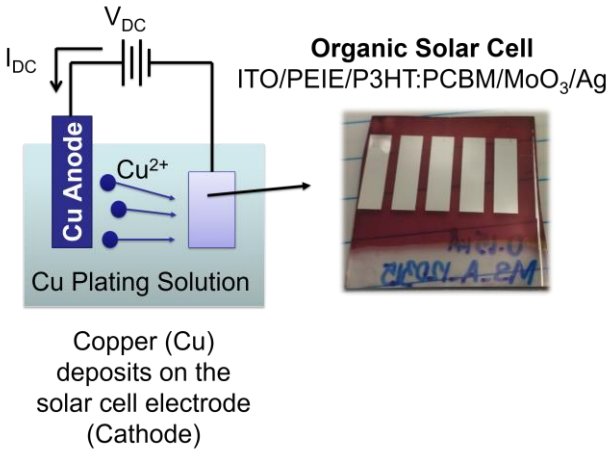

Figure 13. Setup of electrodeposition process using Cu plating solution that will be deposited on the organic solar cell.

Current density – voltage (J-V) characteristics were measured in ambient air using a source meter (Keithley 2420) in a four-wire connection scheme. A solar simulator (TriSol TSS-156, Class AAA, Newport Oriel) equipped with a 1000W Xenon arc lamp with an air mass (AM) 1.5 filter and providing an irradiance of 100 mW/cm^2 was used as the light source. A Si reference cell (2cm × 2cm OAI verified mono-Si reference cell) was used to calibrate the intensity of the solar simulator and the electronic measurement equipment. The structure of organic solar cells and the complete device are shown in Fig. 12 (e). The surface of ITO was modified with PEIE in order to reduce its work function, thus enabling it to act as an electron collection electrode [44]. Fig. 14 (a) shows the current density – voltage (*J-V*) characteristics of solar cells with 30 nm of Ag top electrode tested before- and after-electroplating copper. Under 100 mW/cm^2 of AM 1.5G illumination, the device before the electroplating of copper displays V_{OC} = 0.64 V, J_{SC} = 7.7 ± 0.5 mA/cm^2, and FF = 0.40 ± 0.00, yielding a power conversion efficiency (PCE) = 2.0 ± 0.1 % (Table 4). Averages and standard deviations were based on measurements of 2 devices.

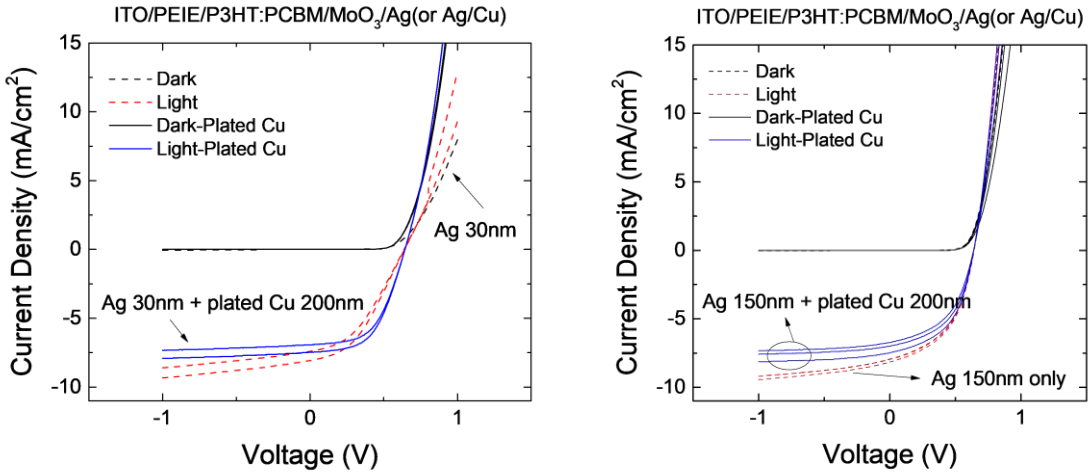

Figure 14. Current density – Voltage (J-V) characteristics of inverted organic solar cells with- and without electroplated Cu top electrode when Ag thickness is (a) 30 nm, and (b) 150 nm.

Compared to the device without Cu-plating, the Cu-plated device exhibits improved overall performance due to a significant decrease and increase of R_SA (28.2 vs. 10.7 Ω-cm^2) and *FF* (0.40 vs. 0.54), respectively. R_SA is the equivalent series resistance of the solar cell, indicating the level of difficulty to extract charge carriers from the solar cells. Therefore, it is preferred to have a lower value of R_SA for the higher fill factor. A reduction of more than half of magnitude was achieved for R_SA, thereby improving *FF* by 35 %. This improvement is attributed to the increased top electrode thickness (Ag 30nm vs. Ag 30nm / Cu 200 nm), thereby increasing the conductance of the top electrode significantly.

Table 4. Summary of OPV parameters with and without electroplated Cu

Top Electrode Configuration	J_{SC} **(mA/cm^2)**	V_{OC} **(V)**	***FF***	R_SA **(Ω-cm^2)**	**η (%)**
Ag 30nm	7.7 ± 0.5	0.64 ± 0.00	0.40 ± 0.00	28.2 ± 7.3	2.0 ± 0.1
Ag 30nm + Cu 200nm	7.2 ± 0.4	0.64 ± 0.00	0.54 ± 0.01	10.7 ± 0.0	2.5 ± 0.1
Ag 150nm	9.2 ± 0.1	0.64 ± 0.00	0.49 ± 0.00	16.5 ± 0.3	2.9 ± 0.1
Ag 150nm + Cu 200nm	8.1 ± 0.4	0.64 ± 0.00	0.50 ± 0.01	18.3 ± 2.1	2.6 ± 0.2

Meanwhile, J_{SC} decreases by 6.5% (7.7 vs. 7.2 mA/cm^2) and this reduction could be due to the interaction between copper plating solution and the photoactive layer of P3HT:PCBM as the entire photoactive regions were submerged during the plating. Although 30nm of Ag protects the photoactive regions from the copper plating solution, the solution can still diffuse into the active layer through the edge of Ag electrode, as shown in Figure 15.

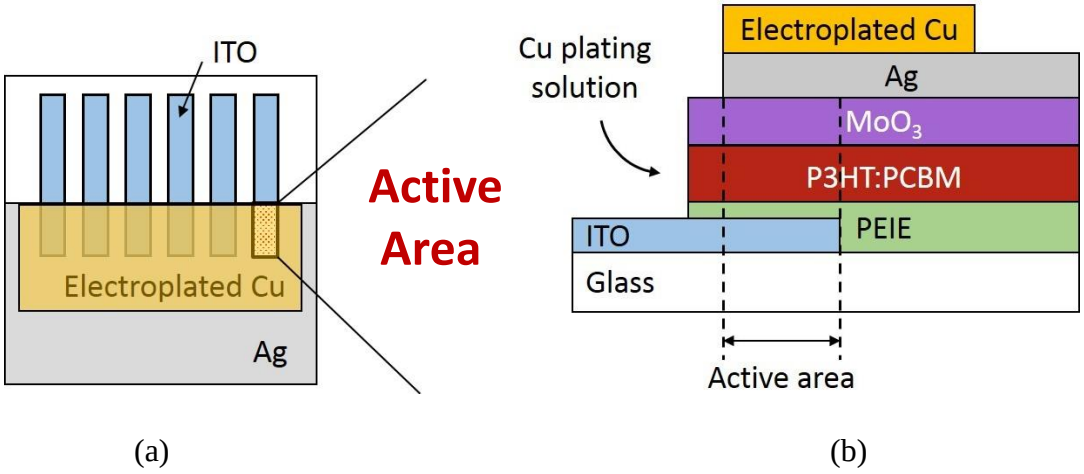

Figure 15. Device geometry of an (a) inverted OPV with the top electrode comprise evaporated silver and electroplated copper, and (b) cross sectional structure. Although 30nm of Ag protects the photoactive regions from the copper plating solution, the solution can still diffuse into the active layer through the edge of silver electrode.

In contrast, Fig. 14 (b) shows the current density – voltage (*J*-*V*) characteristics of solar cells with 150 nm of Ag top electrode tested before- and after-electroplating copper. The device before the electroplating of copper shows V_{OC} = 0.64 V, J_{SC} = 9.2 ± 0.1 mA/cm^2, and *FF* = 0.49 ± 0.00, yielding a power conversion efficiency (PCE) = 2.9 ± 0.1 % (Table 4). Because of thicker Ag (150 nm vs. 30 nm), *FF* improves significantly (0.49 vs. 0.40). Furthermore, J_{SC} is increased as well (9.2 vs. 7.7 mA/cm^2), most likely owing to the enhanced reflectance from the thick (150 nm) Ag.

Compared to the device without Cu-plating (Ag 150 nm only), the Cu-plated device exhibits decreased J_{SC} by 12% (9.2 vs. 8.1 mA/cm^2), again due to the interaction between electroplating solution and the photoactive organic semiconductors. There was almost no improvement in *FF* (0.50 vs. 0.49) since the 150 nm of Ag already provides highly conductive current path for hole collection. Hence, the PCE decreases from 2.9 % to 2.6 %. Therefore, in this work, results have demonstrated improved performances of an inverted OPV by plating Cu on the top Ag electrode. The *FF* is increased by 35% by plating 200 nm of Cu on top of 30 nm of Ag. However, J_{SC} is decreased by 6.5% and this reduction could be due to the interaction between copper plating solution and the photoactive layer of P3HT:PCBM. Despite the decrease of J_{SC}, the PCE increased by 25% thanks to the significant increase of *FF*.

To conclude this experiment, the device with 150 nm of Ag electrode showed decreased PCE after plating Cu due to the decreased J_{SC} and nominal increase of *FF*. The addition of the Cu electrode to the existing thick Ag electrode (150 nm) did not improve the *FF* since the 150 nm of Ag already provides highly conductive current path for hole collection.

3.2 Design and Fabrication of Wrinkled Surfaces

Wrinkled surfaces are generally created through the mechanics of stretching and compressing of thin films [45] and has become of great interest in a wide range of applications, including organic light emitting diodes [46], flexible electronics [39, 47], [39, 47], muscle cell alignment [48], thin film metrology [45, 49, 50], and microfluids [51]. While there are various methods to induce compressive stress, three main methods include mechanically induced wrinkling [45, 52], swelling induced wrinkling [53], and thermally induced wrinkling [54]. Mechanically-induced wrinkling involves hardening the surface of the polymer while the polymer is stretched [45]. The polymer is then released from tension, thereby developing wrinkles on the

surface. In swelling-induced wrinkling, wrinkles are generated by means of swelling the polymer [53]. The surface is first hardened via ultraviolet (UV)-ozone treatment, followed by solvent vapor treatment. During this treatment, the solvent diffuses into the polymer, causing the polymer to swell, thus inducing wrinkles. Lastly, in thermally-induced wrinkling, a hard layer, typically a metal, is deposited at elevated temperature on top of a soft layer, which is typically a polymer [54]. After deposition, the sample cools down, and thermal stress results in wrinkling. Wrinkling is well-known with a number of polymer materials, such as polydimethylsiloxane (PDMS) [48, 51], polystyrene [55], and SU-8 epoxy polymer [53, 56].

The following section describes how a wrinkled surface can be processed and fabricated to uniquely change the height and wavelength of the roughness profile via thermal evaporation; hence, the use of thermally-induced wrinkling in my research. Characterization and analyzation of the fabricated wrinkled surface are also addressed in detail.

3.2.1 Description of Wrinkle Formation and Characterization

In this research, wrinkles are generated by use of thermal stress between a soft layer and a hard layer. An epoxy-based negative photoresist, SU-8, is used as the soft layer, and metal is used as the hard layer. I focused on generating wrinkles by changing parameters involving SU-8 dryness and metal deposition. For SU-8 dryness, the parameters that contribute to wrinkle generation are: annealing temperature, annealing time, and SU-8 spin speed. For metal deposition, the type of metal, deposition rate, metal thickness, and cooling time contribute to generating wrinkles. These parameters were investigated for wrinkle generation, as summarized in Fig. 16. Each testing of parameter determines how the height and period of the textured surface can be uniquely manipulated. Two methods were experimented: (1) generating wrinkles after metal deposition, and (2) generating wrinkles before metal deposition.

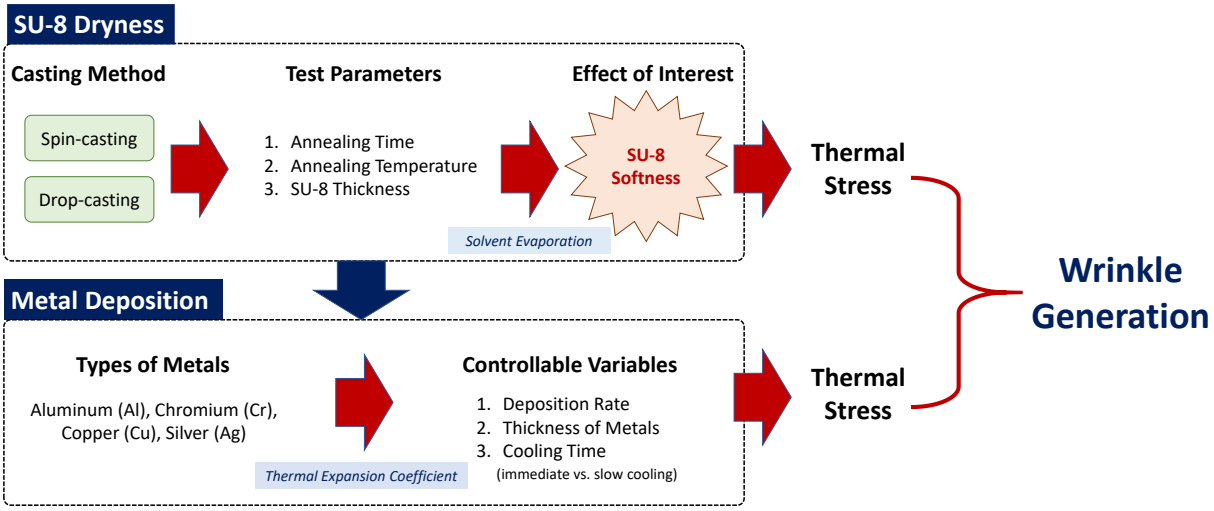

Figure 16. Summary of parameters to generate wrinkles via thermal stress by use of SU-8 dryness and metal deposition.

Performing a thermally-induced method of generating wrinkles requires a hard layer being deposited over a soft layer with respect to increased temperature. This process utilizes the thermal expansion coefficient (CTE), which is a thermal property of a material measuring how much a material expands when it is heated (ppm/˚C = parts per million/temperature in Celsius). It is a known property of materials that heat added to the material will cause the material to expand. Therefore, the next step in this research was to explore how different metals with different CTEs affect the wrinkle generation via thermally-induced wrinkling.

The surface roughness of a wrinkled sample is characterized by measuring its profile using a profilometer. Figure 17 illustrates the surface profile characterization.

1. **Primary profile (P parameter)**

   The profile measured by a stylus often includes significant noise which is called total profile. The primary profile (P) is obtained by applying a proper filter to remove the noise. As can be seen in Fig. 17, the primary profile may include a waviness in addition to surface roughness.

2. **Roughness profile (R parameter)**

In order to obtain the surface roughness from the primary profile, a high pass filter is applied to remove waviness which has a relatively low frequency.

3. **Waviness profile (W parameter)**

For some applications, knowing the waviness is useful and the waviness profile can be obtained by removing the roughness profile from the primary profile by applying a high pass filter.

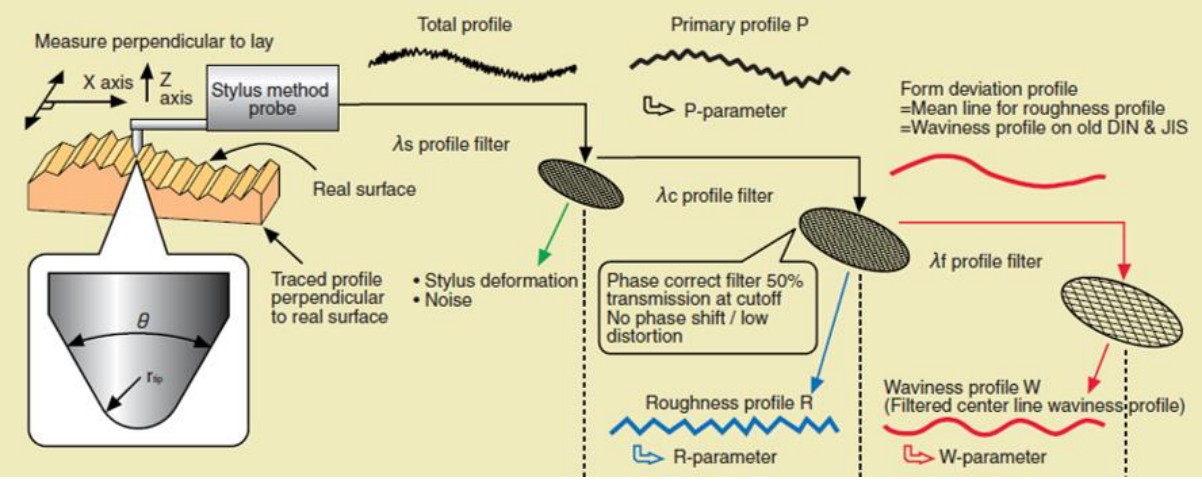

Figure 17. Characteristics of wrinkle profile

In this research the roughness profile (R parameter) is more appropriate to characterize the textured surface since it represents the wrinkle profile that will enhance light trapping and it is obtained by filtering out the initial noise generated from the primary profile (P parameter). An average value is useful for characterizing the roughness of a wide area (Equation (3)). This value is obtained by averaging the absolute deviation from the mean line over one sampling length as shown in Fig. 18.

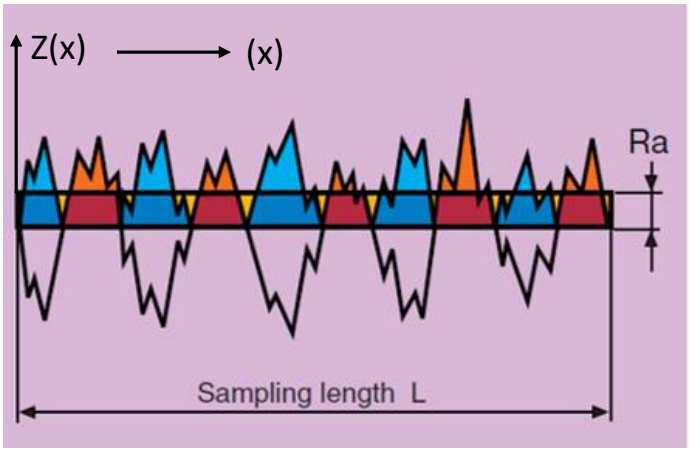

Figure 18. Average surface roughness

$$R_a = \frac{1}{n} \sum_{i=1}^{n} |Z_i| \quad (3)$$

3.2.2 Optimum Wrinkle Generation for Organic Solar Cells

There have been tremendous interest generating wrinkles for organic solar cells, as light harvesting techniques and methods advance. Such work incorporates numerous light manipulation strategies, such as geometric optics [8-10, 17, 24], photonic nanostructures [57-59], gratings [60, 61], reflective and anti-reflective coatings [60], micro-structured scattering layer [62], and surface texturing [63]. Wrinkles for organic solar cells can also be generated from other methods, such as mechanical compression [64], or thermal annealing [65]. Unique approaches have also been demonstrated with the use of special materials such as fossilized diatoms, also known as diatomaceous earth [63]. Kim et al. utilized a conventional structure with P3HT:PCBM bulk heterojunction polymer, and demonstrated a power conversion efficiency of 1.8% with the use of wrinkles via compressive stress and modifying the irradiation time of UV exposure [64]. However, an improved efficiency of 2.1% was performed with the use of a composite surface, which incorporates deep folds in addition to wrinkles. Despite a 14% improvement, the focus of generating wrinkles and folds were only concentrated on optimizing

the wavelength period, which ranged from 1.2 um to 5.0 um. Lampande et al. fabricated an inverted structure using PTB7Th:PCBM active layer, and demonstrated an efficient light harvesting technique by fabricating a PDMS micro-structured scattering layer (MSL). The PDMS mold was fabricated using facile roll-to-roll process and mold transfer method [62]. This method resulted an efficiency of 8.60% compared to a device with no MSL with efficiency of 7.53%, indicating a 12% improvement. However, the light-trapping structure incorporates an ordered hemispherical structure rather than a random wrinkle profile. Current research has also focused to realize the potential of printing organic solar cells with wrinkles or similar light-trapping structures due to its flexibility. For example, Yun et al. demonstrated a bendable organic solar cell that produced an efficiency of 7.4% by coating a light-scattering silica nanoparticle layer (SNL) onto a polymer substrate [58], enhancing light absorption of the photoactive layer, thus increasing photocurrent generation. The photoactive layer thickness also reduced by 30%, which reduces excess material, making this a cost-effective process while being highly-throughput. An additional example regarding printing organic solar cells includes Mayer et al. demonstrating an 11% power conversion efficiency enhancement of a printed organic solar cell, where prior work only delivered below 7% efficiency enhancement [59]. A photonic nanostructure is embedded in a transparent film, which allows flexibility and a great conformal device attachment. Bi et al. utilized a periodic grating via holographic lithographic lithography technique to fabricate a 2D dual periodic corrugation into the metallic electrodes to demonstrate a significant efficiency improvement of 31% [61]. The stated methods of generating wrinkles and light trapping structures are summarized in Table 5.

Table 5. Summary of generating wrinkles and light trapping methods for solar cells

Author	Light Trapping Example	Wrinkle or Light Trapping Profile	Photoactive Layer	Method to Induce Wrinkles or Light Trapping Structure	Efficiency Enhancement Compared to a Planar Device
Cho et al. [24]	Random and V-groove texturing for OPVs	V-groove textured film period: 50 um Vertex angle: 100˚	PCDTBT:PCBM	Geometric light trapping (textured PDMS film is laminated on backside of glass substrate)	13.8%
Kim et al. [64]	Wrinkles and deep folds for OPVs	Period: 1-5 um Peak-to-valley: 180 nm	P3HT:PCBM	Mechanical compression	14%
Yun et al. [58]	Bendable OPV	Relative scale of diameter, height, interparticle distance: 4:6:7 in 570 nm thick SNL	PTB7:PCBM	Silica nanoparticle layer (SNL)	13.5%
Mayer et al. [59]	Printed OPV	Period: 500 nm Depth: 700 nm	D4610:PCBM	Photonic nanostructure	11%
Bi et al. [61]	2D Dual-periodic corrugation for OPVs	Groove depth:70 nm (1D) and 60 nm (2D) Grating period: 350 nm (2D dual period)	SubPc:C_{60}	Periodic grating (holographic lithography technique)	31%
Lampande et al. [62]	Hemispherical structures	Diameter: 80 um Height: 50 um (each structure separated by distance of 7 um)	PTB7-Th:PCBM	Micro-structured scattering layer (MSL)	12%
McMillon-Brown et al. [63]	Processing nanostructured diatomaceous earth (DE) for polymer solar cells	Average DE particle size integrated in solar cells: 250 nm (DE size was reduced from 8 um wide and 20 um long by ball milling)	P3HT:PCBM	Treated DE particles are added to DCB solution when dissolving P3HT:PCBM solution	30%

Based on Table 5, it is observed that the greatest efficiency improvement is demonstrated by Bi et al. Generating this type of corrugated profile consists of two different periodic gratings into the metallic electrodes by holographic lithography technique. This allows and promotes effective broadband light trapping in organic solar cells, thereby extending the wavelength region of the enhanced light absorption. Incorporating the dual periodic corrugation also enhances surface plasmon-polariton (SPP) effects, which are infrared or visible-frequency electromagnetic waves that travel along the cathode (Al)/organic interface (SubPc:C_{60}) in broadband wavelength region. By tuning the periods of the microstructures, the SPP resonance in corrugated cathode/organic interface can also be tuned. However, this method focuses on an ordered light trapping structure. Modifying the microstructures only allows an ordered, fixed dimension, thus limiting light trapping enhancement throughout the whole surface. Similarly, other authors demonstrated how their light trapping structures and wrinkled surfaces are limited to a certain degree of period or depth by utilizing complex fabrication process or entirely unique materials. Therefore, I will fabricate a randomly corrugated, wrinkled surface, using photoactive layer with P3HT:PCBM, generating wrinkles through simple process of using compressive forces. SU-8 will be used as a soft polymer, while popular metals, such as Al, Cr, and Cu will be used as a hard layer. This process not only utilizes simple fabrication methods, but as well as fine tuning the wrinkle profile through the use of controlling the SU-8 softness via thermal and solvent annealing.

In order to make an efficient light trapping structure for organic solar cells, wrinkles should have large average roughness, R_a. However, if the surface is too rough, producing very sharp peaks with narrow periods, then fabricating organic solar cells on top of this structure will become significantly difficult. In contrast, if the surface is nearly smooth (very fine roughness), leaving

very little height and wide periods, there is little-to-no light trapping. Therefore, in this work, I carefully designed and conducted a series of experiments to find an optimum wrinkle profile that balances the trade-off between easiness of solar cell fabrication and light trapping efficiency. I have tried three different methods to generate wrinkles, which are based on the thermally-induced wrinkling method: (1) Method 1 – Wrinkle generation on a thin SU-8 after metal deposition, (2) Method 2 – Wrinkle generation on a thick SU-8 after metal deposition, and (3) Method 3 – Wrinkle generation on a thick SU-8 before metal deposition.

Method 1: Wrinkle generation on a thin SU-8 after metal deposition

In this method, metal is thermally evaporated on top of a soft polymer layer in a high vacuum chamber. The temperature of the metal and polymer layers change significantly during deposition. As temperature decreases after deposition, metal and polymer layers start to shrink with different rates, depending on the Coefficient of Thermal Expansion (CTE). CTE describes how the size of an object changes with change in temperature at a given pressure. In order words, it measures the fractional change in size per degree change in temperature at a constant pressure. One dimensional (length) change is widely used to measure the change in size, and in this case a coefficient of linear thermal expansion is used. The Table 6 lists common thermal expansion coefficients for various materials.

Table 6. Coefficients of thermal expansion (CTE) of various materials

Metals	**CTE [ppm/°C]**	**Polymers**	**CTE [ppm/°C]**
Aluminum (Al)	23.6	**PDMS**	300
Copper (Cu)	16.5	**Kapton**	20
Chromium (Cr)	6.2	**SU-8**	52
Silver (Ag)	18	**Carbon Fiber**	-0.8

For proper wrinkle generation, the polymer layer must be soft enough to induce wrinkles, hence the dryness of the polymer is a major parameter in addition to the CTE differences to optimize the wrinkle profile. In this research, SU-8 polymer is used as a layer for wrinkle generation along with various metals. First, a glass slide is cleaned with acetone and isopropanol sonication, followed by deionized (DI) water rinse. SU-8 polymer is spin-coated and annealed on a hotplate. Once the SU-8 is cured, it is transported in the thermal evaporator to deposit a metal. The deposition takes place at high vacuum in order to deposit a high purity metal, typically at a pressure less than 3×10^{-6} Torr. The dryness of the SU-8 polymer depends on the film thickness and thermal annealing conditions. In this experiment, I fixed the thermal annealing condition and varied the spin coating speed, thereby producing different SU-8 thicknesses. Thinner film is harder to achieve than thicker film at a given thermal annealing condition. Fig. 19 summarize the fabrication process.

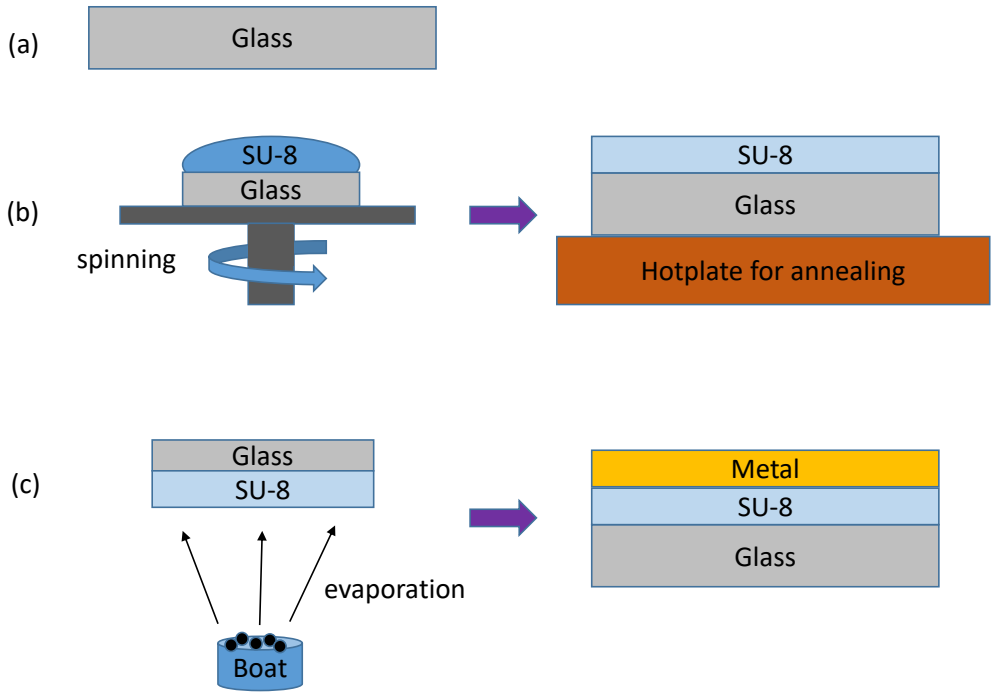

Figure 19. Fabrication process for the method 1. (a) Cleaning of glass substrates, (b) SU-8 spin coating, (c) Annealing of SU-8, and (d) Evaporation of metal in a high vacuum chamber.

Three different spinning speeds were used: 1000, 2000, and 3000 rpm to control the dryness of the SU-8 and three different metals were used to induce wrinkles: aluminum, chromium, and copper. These cases are summarized in the Table 7.

Table 7. Summary of process parameters with images of wrinkles and average roughness. All samples were annealed for 3 minutes at 95˚C on a hotplate to dry the SU-8 layer.

Metal		**SU-8 Spin Speed (SU-8 3010) CTE = 52 ppm/˚C**		
		1000 rpm	2000 rpm	3000 rpm
Aluminum (Al) CTE = 23.6 ppm/˚C	Optical images	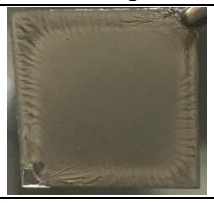	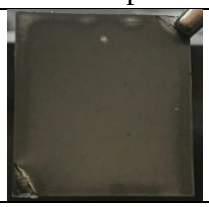	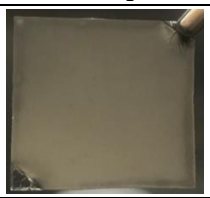
	Roughness (R_a) [µm]	4.2	1.9	1.3
Chromium (Cr) CTE = 6.2 ppm/˚C	Optical images	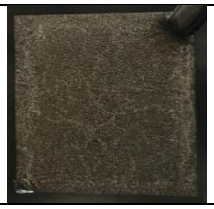		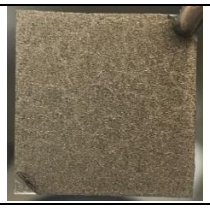
	Roughness (R_a) [µm]	3.3	3.7	5.0
Copper (Cu) CTE = 16.5 ppm/˚C	Optical images			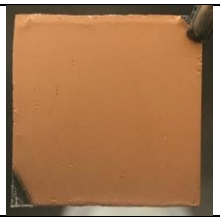
	Roughness (R_a) [µm]	0.7	1.0	0.5

As can be seen in the table, the surface morphologies depend on film thickness as well as on species of metal. Devices with chromium exhibit a very rough surface while devices with copper exhibit a very fine wrinkle profile. To gather quantitative data, all samples were scanned with a surface profilometer. Figures 20 – 22 show surface profiles of samples with aluminum,

chromium, and copper, respectively. Each graph overlaps profiles of wrinkles acquired from different SU-8 thicknesses at different spin speeds in rpm. The average roughness was measured as listed in the Table 7.

Following are observations from this experiment:

a. For the device with aluminum, the roughness decreases as the SU-8 spin speed increases. Higher spin speed produces a thinner SU-8 film and becomes harder than thicker film at the same annealing condition. Hence, change in volume of the thinner SU-8 becomes more difficult and that's why the roughness decreases as the SU-8 becomes thinner.
b. For the device with chromium, the opposite trend is observed; the roughness increases as the SU-8 spin speed increases. This is due to the increase in differences of CTEs for chromium and SU-8. ΔCTEs for the Al/SU-8 and the Cr/SU-8 are 28.4 and 45.8 ppm/˚C, respectively. As SU-8 becomes thinner, i.e., harder, the increase in CTE difference develops cracks in SU-8. In harder films, when an excessive stress is applied, the film is not considerably deformed, but rather cracks are developed as shown in the images in Table 7.
c. For the device with copper, the smoothest surface is obtained compared to the other two metals. Based on the observations in sections *a* and *b* above, the surface roughness for the device with copper should lie between that of the device with aluminum and the device with chromium. Furthermore, no consistent trend was found with increasing spin speed. I plan to repeat the experiment for the device with copper deposition to validate this observation.

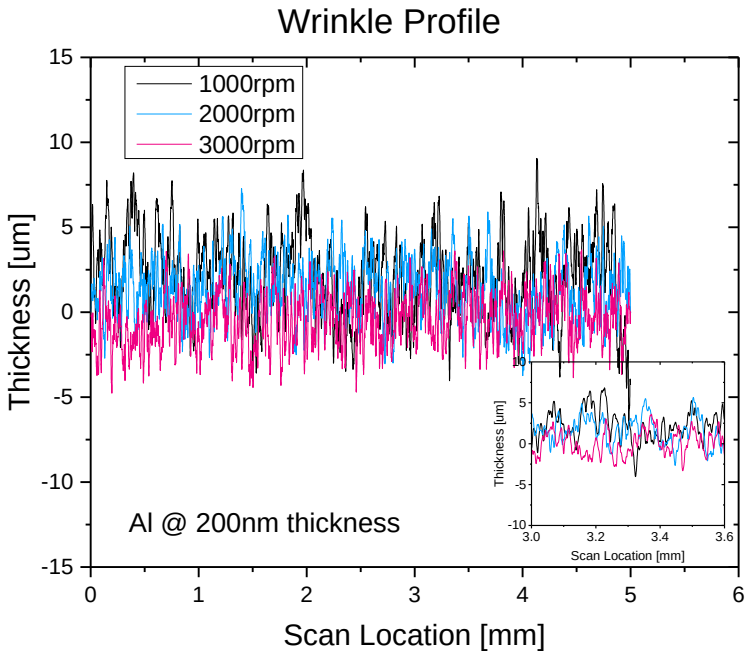

Figure 20. Wrinkle profile for aluminum 200 nm. Scan length is 5 mm and the inset shows wrinkle profile of scan length between 3 and 3.6 mm.

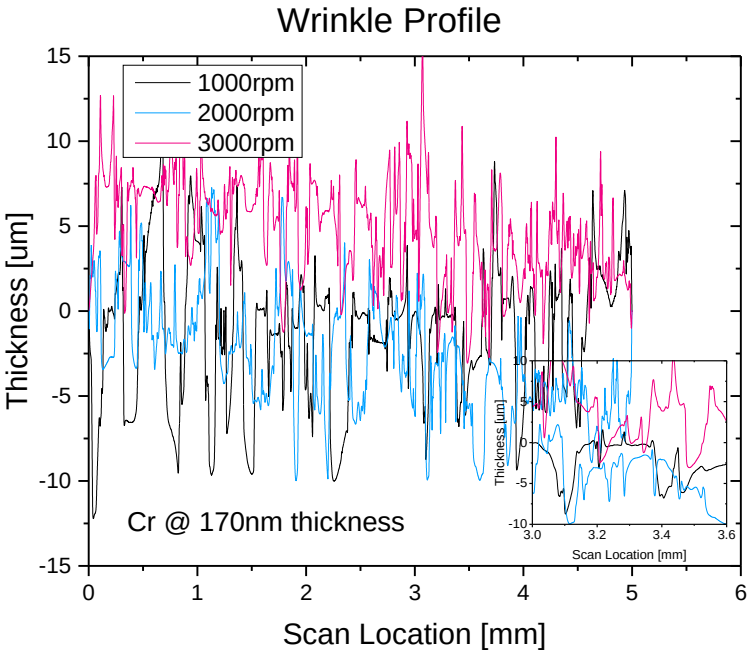

Figure 21. Wrinkle profile for chromium 170 nm. Scan length is 5 mm and the inset shows wrinkle profile of scan length between 3 and 3.6 mm.

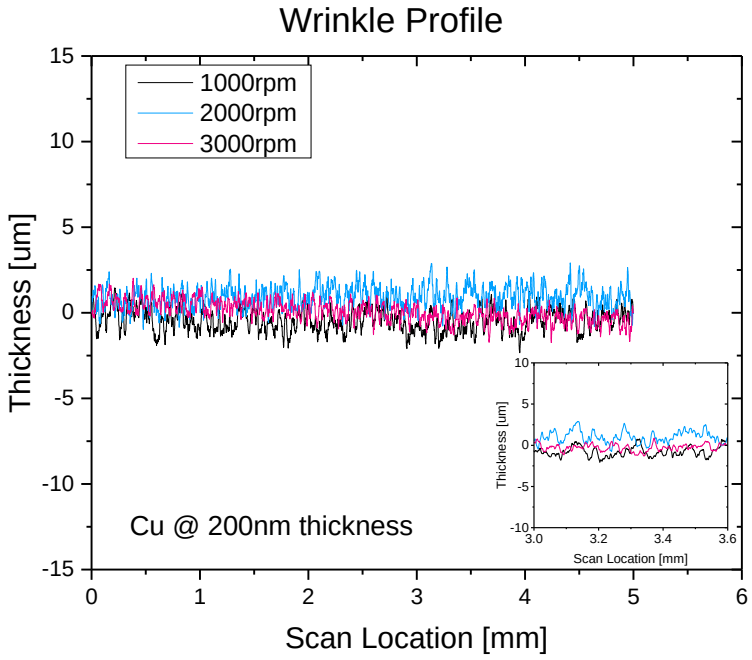

Figure 22. Wrinkle profile for copper 200 nm. Scan length is 5 mm and the inset shows wrinkle profile of scan length between 3 and 3.6 mm.

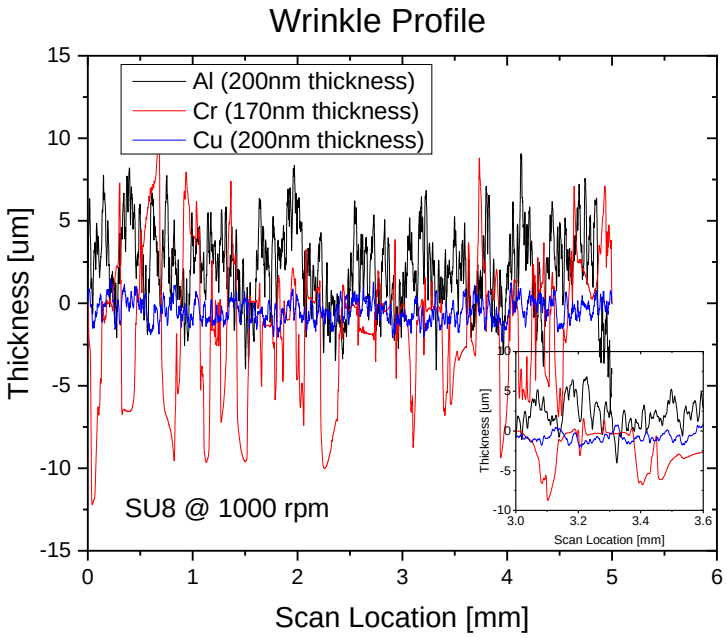

Figure 23. Wrinkle profiles obtained from samples with different metals at a given SU-8 thickness (1000 rpm). Scan length is 5 mm and the inset shows wrinkle profile of scan length between 3 and 3.6 mm.

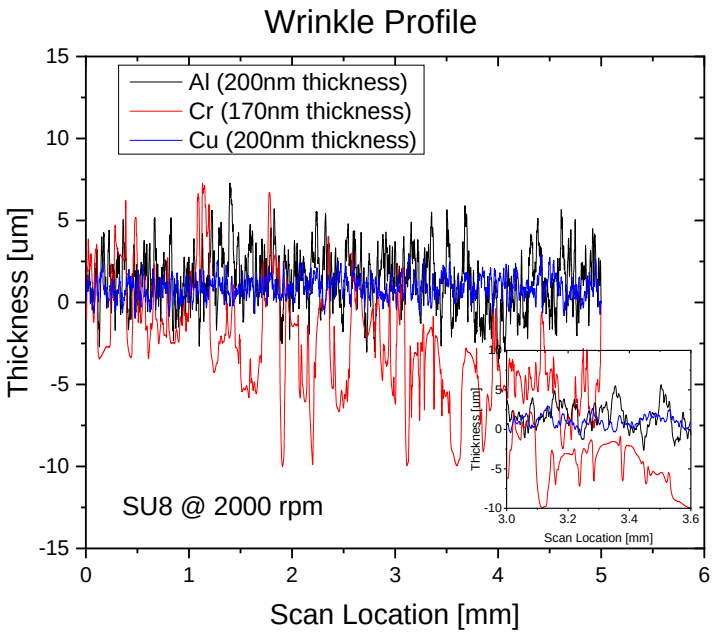

Figure 24. Wrinkle profiles obtained from samples with different metals at a given SU-8 thickness (2000 rpm). Scan length is 5 mm and the inset shows wrinkle profile of scan length between 3 and 3.6 mm.

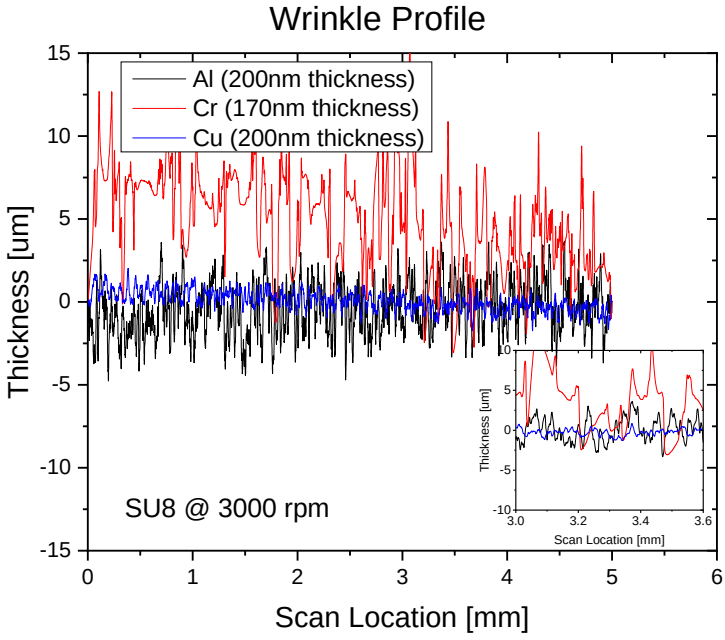

Figure 25. Wrinkle profiles obtained from samples with different metals at a given SU-8 thickness (3000 rpm). Scan length is 5 mm and the inset shows wrinkle profile of scan length between 3 and 3.6 mm.

During another experiment I observed that much larger wrinkles can be created when the SU-8 film is very thick. For example, SU-8 film thickness is typically thicker in the edge than the center area due to the nature of the spin-coating technology. In order to confirm this, I made a new device with SU-8 3025 and silver electrode for a much thicker film, promoting an increased roughness. Viscosities of SU-8 3025 and SU-8 3010 are 4400 and 340 centistokes (cSt), respectively [66]. Hence, SU-8 3025 produces a much thicker film compared to SU-8 3010 at a given process conditions. According to the data sheet of the SU-8 3000 series polymer (or photoresist), SU-8 3025 can be coated with 25 μm of resist [66]. Because of the thick resist, a coating process must be carefully established to achieve a desired thickness. Spin-casting creates a centripetal force in the center of the sample, moving excess resist to the outer edges. With thicker resists, such as with SU-8 3025, the centripetal force 'pushes' the excess towards the edges, resulting in rather thicker layers on the edges compared to the center. This process is followed by a soft baking process. Since the outer edges are thicker, they tend to be 'softer' (solvent is not fully evaporated), compared to the center region (more solvent in this area evaporated due to thinner film). Upon metal (Ag) deposition, a thermally-induced method of generating wrinkles becomes easily attainable on the edges. SU-8 3025 was spin-coated at 3000 rpm for 30 seconds on a glass substrate and annealed on a hotplate at 95˚C for 5 minutes followed by 200 nm of silver (Ag) deposition. With this process parameters, the device exhibited much thicker edge build-up of the SU-8 which was still soft compared to the center area. This is clearly shown in the image in Fig. 26 where wrinkles are primarily concentrated along the edge where the SU-8 is still soft. The wrinkle profile also confirmed this as the edge area exhibited 2.0μm of roughness while the center area showed a near perfect smooth surface. Comparing the wrinkle profiles of the thin SU-8 (SU-8 3010) and the thick SU-8 (SU-8 3025), no significant

difference in average roughness was observed confirmed by Fig. 27. However, there is a distinct difference in the wrinkle period which is defined as the average distance between peak to peak along the scan direction. Wrinkles from the thin SU-8 layer resulted in a good wrinkle profile with adequate height. However, the height difference either displays peaks that are too sharp (which makes solar cell fabrication significantly difficult), or a profile that is too fine (which provides very little light trapping). Attainment of peaks that are not too sharp or a profile that is not too fine (but not both) are sufficient for this research. The device with a thicker SU-8 layer shows a wider period which is preferable for the easy fabrication of thin-film organic solar cells on top of the wrinkles. Hence, my next experimental method focused on wrinkle generation on a thick SU-8 layer.

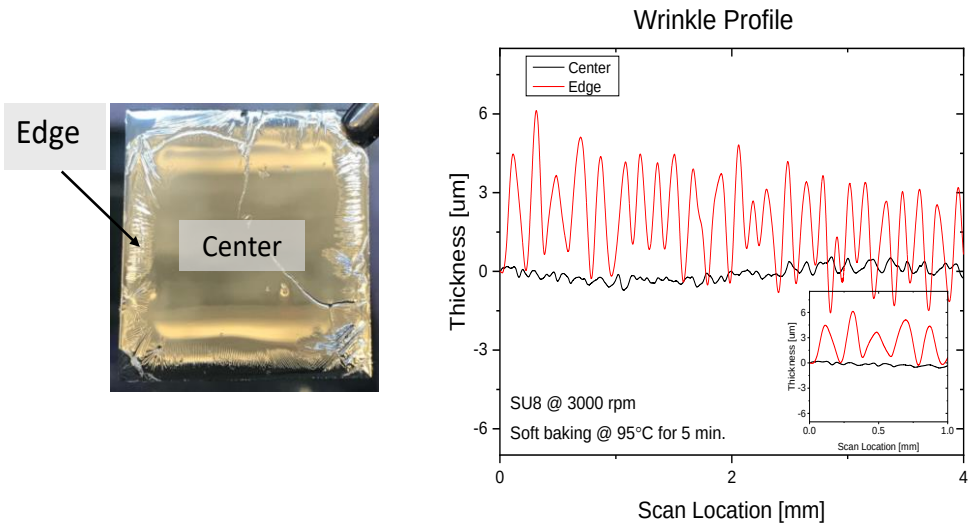

Figure 26. Roughness profile of wrinkling at edge and center surface with a roughness of 2.03 um

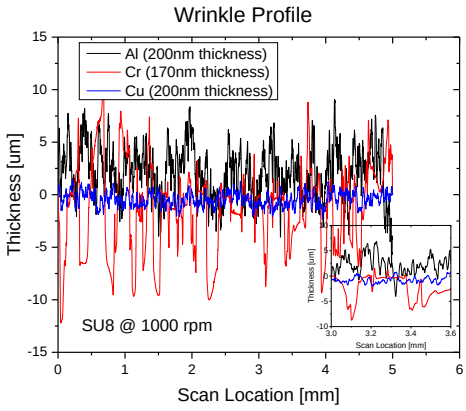

(a) Wrinkles from the SU-8 3010

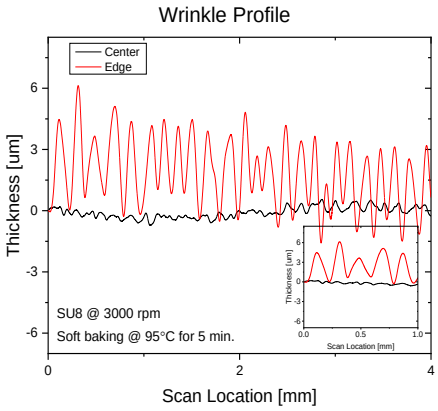

(b) Wrinkles from the SU8-3025

Figure 27. Surface roughness comparison between devices with thin SU-8 and thick SU-8. Although there is not much difference in terms of the average roughness for them, there is a distinct difference for the wrinkle period which is defined as the average distance between peak to peak along the scan direction.

Method 2: Wrinkle generation on a thick SU-8 after metal deposition

In this method, metal is thermally evaporated on top of SU-8 polymer layer in a high vacuum chamber as was the case with Method 1. However, SU-8 3010 is replaced with SU-8 3025 polymer in order to produce a much thicker layer. When spin-coating a much thicker SU-8 film, wrinkles were not produced evenly throughout the whole surface (only the edges produced wrinkles) as shown in Fig. 26 due to unevenness of the thickness. Therefore, in order to achieve a flatter surface of thick SU-8 layer, with a smooth, evenly distributed wrinkle structure, I explored a different casting method known as a drop casting.

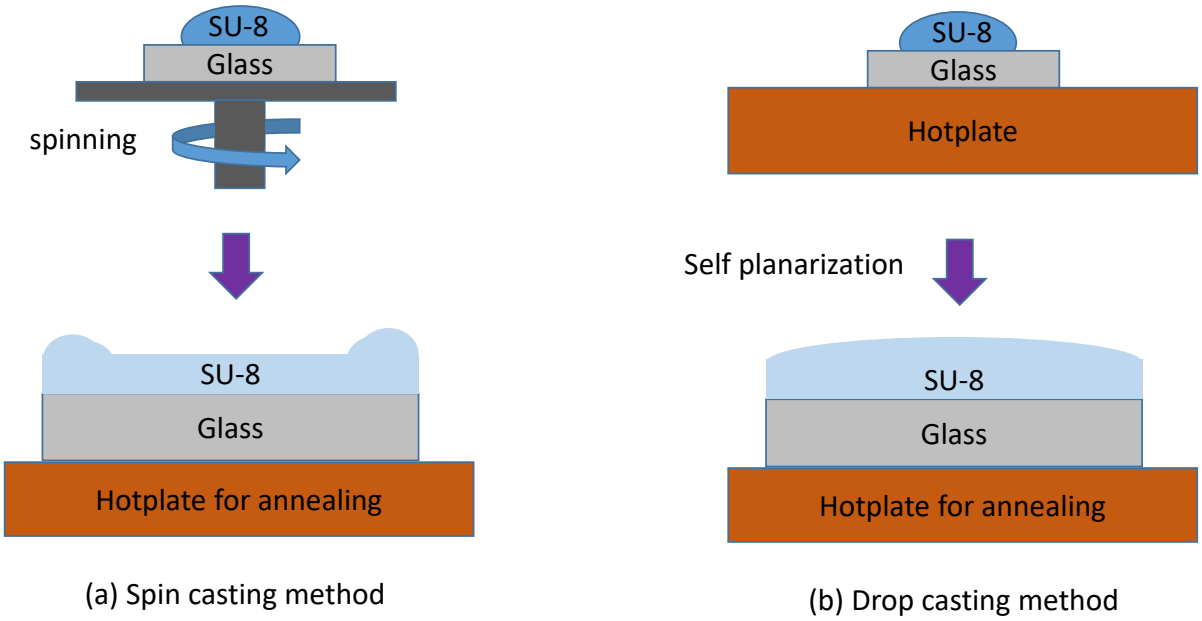

Figure 28. Comparison of (a) spin casting and (b) drop casting. Due to the nature of spinning, spin casting method generally leaves a thick build-up of polymer on the edges. Hence, for a better uniformity of thick polymer layer, a drop casting is preferred. In this method, a solution of polymer is simply dropped on the substrate and planarized by itself on the leveled hotplate.

Due to the nature of spinning, the spin casting method generally leaves a thick build-up of polymer on the edges. Hence, for a better uniformity of thick polymer layer, drop casting is preferred. In this method, a solution of polymer is simply dropped on the substrate and planarized by itself on the leveled hotplate. The thickness of the layer is determined by the amount of SU-8 to dispense and takes longer to dry the SU-8 layer as it contains a significantly more solvent trapped inside thick layer. To check SU-8 for ‘wetness’, a tweezer can be used to touch the corner of the sample during the annealing process. SU-8 is considered ‘wet’ if a dimple is made with a small amount of force, or if the sample is ‘sticky.’ If on the other hand, an incrementally higher force is needed to make a soft dimple, or mark, on the surface without it being sticky, the surface is soft and ready for the metal deposition process.

For this experiment, I attempted drop-casting 0.50 mL of SU-8 3025 onto the 1 inch by 1 inch glass substrate. This method was applied while the glass substrate was on the hot plate to promote self-planarization. Three samples were prepared to find optimum annealing conditions. After dispensing, the samples underwent annealing at 85˚C, but with different annealing times: 4 hours, 6 hours, and 12 hours, followed by depositing 200nm of Ag. However, I found that samples with shorter annealing times (4 and 6 hours) deformed, as the applied heat during Ag deposition melted the rather too soft SU-8 layer, deforming the entire layer, as shown in Table 8. The device with 12 hours of annealing also showed a significant deformation after silver deposition, indicating that more than 12 hours of annealing is required to make an optimum softness of the SU-8 3025.

Rather than pursuing a much longer annealing time, I increased the annealing temperature from 85˚C to 100˚C to expedite the annealing process, while maintaining 0.5 mL of SU-8 3025.

Table 8. Drop-casting SU-8 3025 showcasing deformation with 4, 6, and 12 hours annealing time after Ag deposition.

SU-8 Amount	Annealing Temp.	Annealing Time	SU-8 Surface	Ag Deposition
0.50 mL	85˚C	4 hours	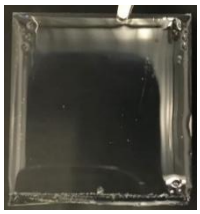	
		6 hours	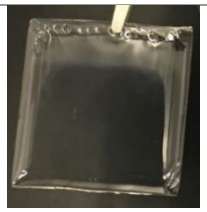	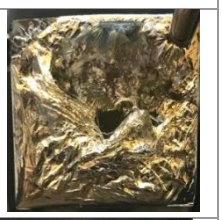
		12 hours	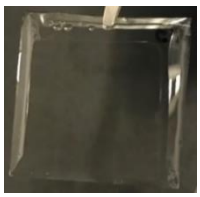	

The new annealing process, at 100˚C for 4 hours, resulted in a hard surface. After depositing 200nm of Ag, the surface was much smoother and very reflected, meaning there was visually little-to-no light trapping. This indicates that the annealing condition is not yet optimized (the hard surface will not produce any wrinkles after metal deposition). However, a unique phenomenon was observed after a few days: wrinkles were generated throughout the surface after 1 week of setting, or cooling down, of the sample slowly.

Fig. 29 shows photos of this transformation at different viewing angles which were taken immediately after Ag deposition and 1 week after Ag deposition. The measured wrinkle profile in the Fig. 29 (e) shows an average roughness of 10.3 μm. However, the average period is about 3 mm which is rather too wide to provide an effective light trapping.

Allowing the sample to set over a longer period promotes a significant increase in average wrinkle roughness, which is more than doubled compared to the thin SU-8 spin-casting devices. Although the SU-8 surface was hard after annealing, there was still enough solvent that had not yet fully evaporated. Therefore, after Ag deposition, during the setting/cooling time, the solvent had a tendency to evaporate. However, because the thick (200nm) Ag film is layered over the SU-8, the SU-8 layer constricts itself underneath Ag while it undergoes a volume change due to the loss of solvent, where Ag is forced to accommodate the shrinking SU-8 layer over time, hence, creating wrinkles.

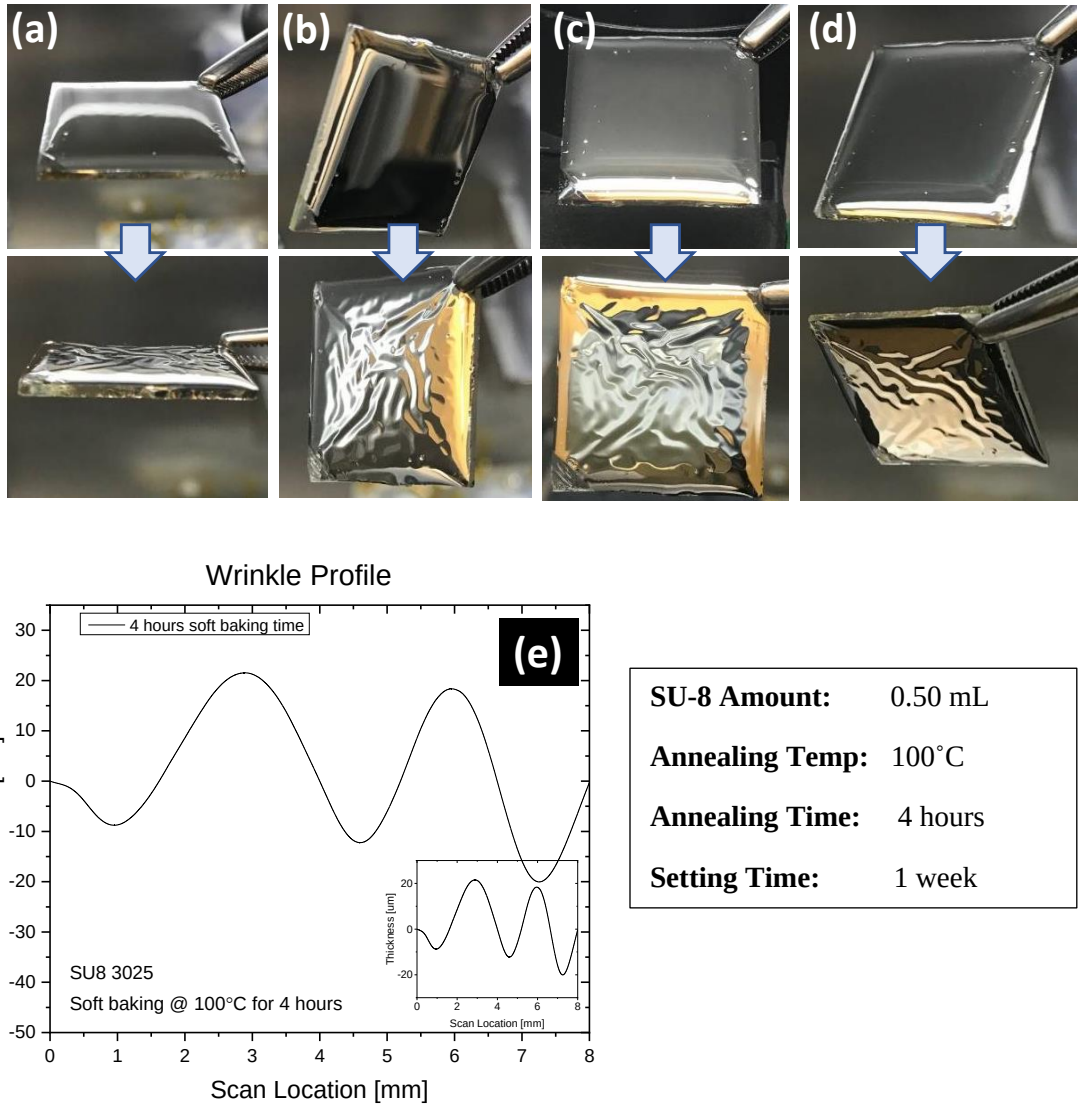

Figure 29. Effect of a combination process of drop-casting, annealing, and setting the sample for 1 week to generate wrinkles. (a) – (d) shows transformation from immediate post-Ag deposition, followed by 1 week setting/cooling. (e) displays its roughness profile.

After completion of this experiment, it was concluded that there was a trade-off between the amount of SU-8 3025 dispensed, and the annealing time. Dispensing 0.50mL, although a guaranteed increased amplitude, requires more optimization time if the annealing temperature is maintained at 100˚C, and possibly an additional parameter of a setting/cooling period. In addition,

maintaining a temperature of less than 100˚C results in melting the SU-8 during metal deposition, as seen in Table 8.

Despite a significant improvement of the wrinkle amplitude, with this method the results are not guaranteed to be reproduced should the setting time vary (i.e., setting for 1 week compared to setting for 1 month). Additionally, this method requires a much longer fabrication process that could hinder research progress should any parameters be modified (i.e., changing SU-8 amount and annealing temperature). Therefore, generating wrinkles after metal deposition resulted in either producing very sharp and narrow peaks (from spin-coating), or in melting the SU-8 or required a much longer processing time. Since an improved wrinkle profile can be achieved for application in solar cells, the next method explores generating wrinkles with increased roughness but within a shorter period.

Method 3: Wrinkle generation on a thick SU-8 before metal deposition

Method 3 differs from the previous two methods as it aims to develop wrinkles before the metal deposition. The advantage of this method is that since the wrinkle is generated and fixed before the metal deposition, the wrinkle profile will not be changed after metal deposition which is a problem with Method 2.

In order to create a uniform thick SU-8 layer, a drop-casting method is used again. Therefore, another attempt was made to dispense 0.15mL and 0.10mL of SU-8 3025 with the use of a mechanical pipette on 1 inch by 1 inch glass substrates. Both samples were annealed at 100˚C and were checked at 4 hours, 8 hours, and 12 hours (using a hot plate timer that provides 1 hour, 4 hours, 8 hours, and 12 hours timer).

The sample with 0.15mL SU-8 3025 showed signs of insufficient annealing after 12 hours (Fig. 30(a)). Since the layer was found to still be wet after 12 hours of annealing, 8 hours

were added to the annealing process while checking at each 4 hour mark (16 hours, and 20 hours), as shown in Fig. 30(b) and (c). At 16 hours, small wrinkles had started to form at the edge and had become more apparent all over the surface after 20 hours of annealing. After a total of 20 hours of annealing, the devices were stored at room temperature for a full week. After a week of setting, the device was annealed on a hotplate at 100˚C for an additional 6 hours (for an accumulate annealing time of 26 hours, Fig. 30 (d)) and the wrinkle profile was observed for any changes. As shown in Fig. 30, wrinkles became more profound after the additional six hours of annealing. After a few minutes of cooling down, all surfaces appeared to be very hard (where little marks could be made by the tweezer and the wrinkle profile remained unchanged).

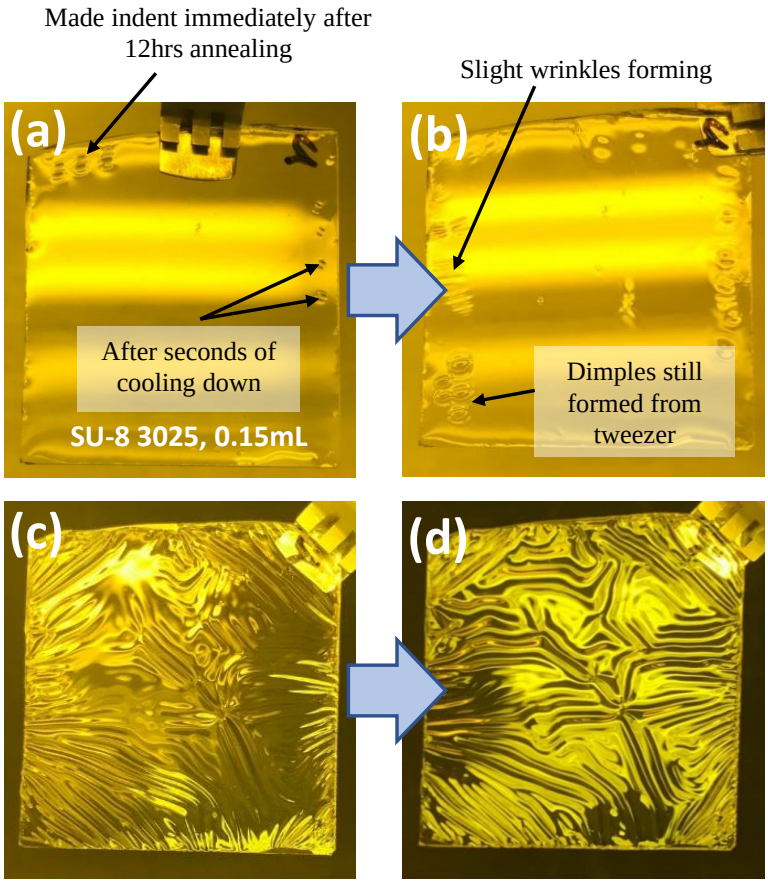

Figure 30. Wrinkle generation of 0.15mL SU-8 annealed at 100˚C with annealing time showing (a) 12 hours, (b) 16 hours, (c) 20 hours, followed by 1 week setting and (d) 26 hours annealing time.

Further experimentation is needed to explain why the wrinkles were generated before metal deposition. It is suspected that a large amount of solvent inside thick SU-8 was unable to evaporate before the surface became completely dry. Hence, the dried surface played a similar role as a metal layer while the solvent evaporated slowly from the deep inside SU-8 layer. This is further illustrated in Fig. 31.

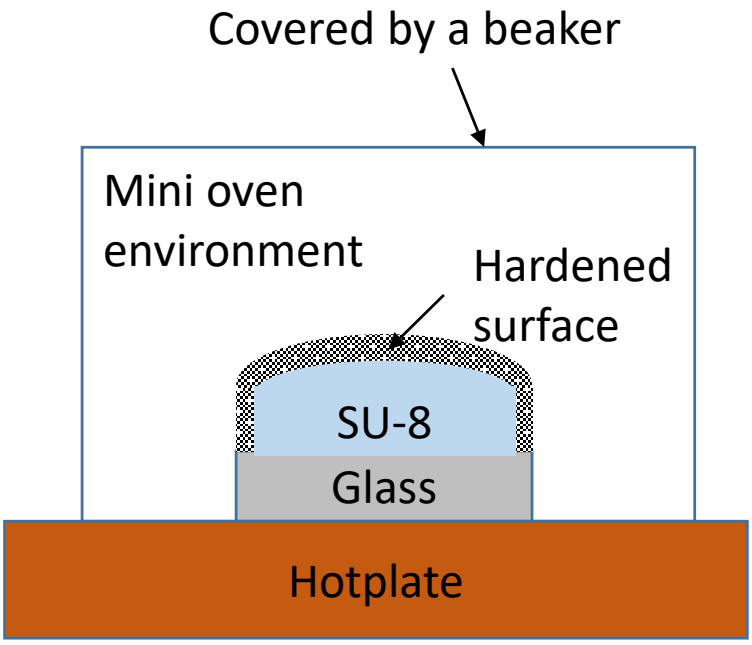

Figure 31. Explanation of wrinkle generation before metal deposition. Due to the mini oven environment, SU-8 surface becomes quickly dried before the evaporation of all solvents trapped deep inside SU-8 layer. The dried surface played a similar role as a metal layer while the solvent evaporates slowly from the deep inside SU-8 layer

Annealing conditions of the previous sample were applied to a sample with 0.10mL SU-8 3025 which is thinner than the previous sample (0.15 mL of SU-8 3025). Compared to the results for the 0.15mL SU-8 sample, finer wrinkles were observed, as shown in Fig. 32. This indicates

that with a thinner polymer layer, more constrictions of the layer occur with the same combination of the annealing time and the setting.

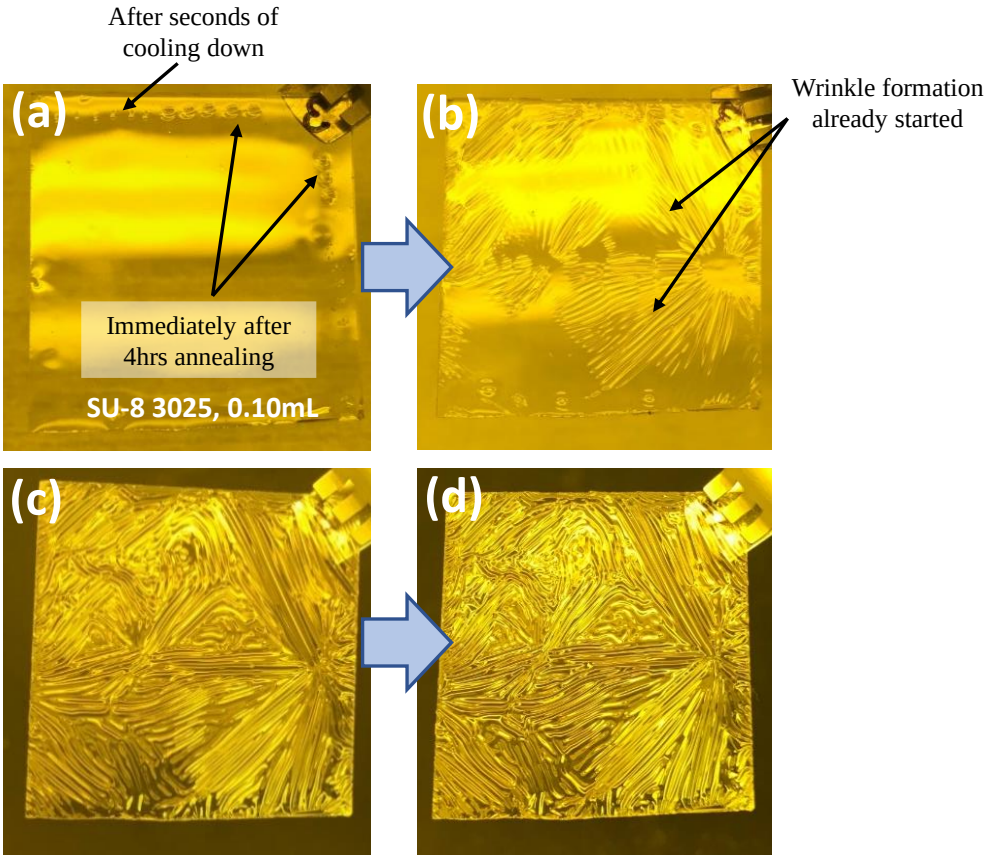

Figure 32. Wrinkle generation of 0.10mL SU-8 annealed at 100˚C combined with setting/cooling time showing (a) 4 hours, (b) 8 hours, (c) 12 hours, followed by 1 week setting and (d) 18 hours annealing time.

The wrinkle scanning profiles of each sample are shown in Fig. 33 (a) and (c), with the scanning locations marked for comparison of different surface areas. The roughness profiles of the samples are shown in Fig. 33 (b) and (d), respectively with the measured average roughness for these samples shown in Table 9.

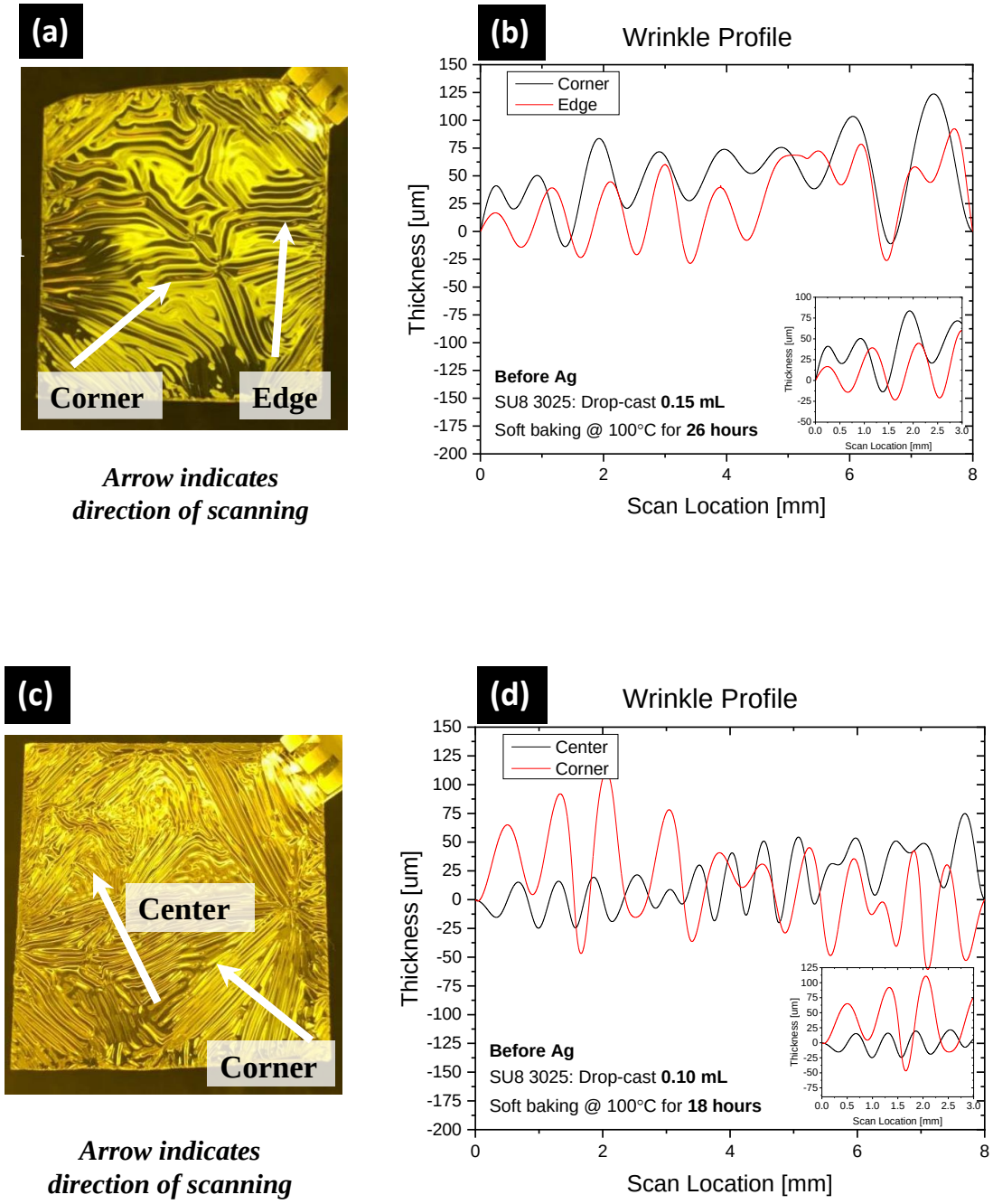

Figure 33. Surface roughness and placement of scanning directions of (a) 0.15mL, and (c) 0.10mL SU-8 3025, displaying roughness profile in (b) & (d) respectively.

To observe changes in wrinkle profile, 200 nm of Ag was deposited. Figures 34 and 35 compare the wrinkle profiles before and after metal deposition for the 0.15mL of SU-8 and the 0.1mL of SU-8 samples. Table 9 summarizes the average roughness before- and after- metal deposition scanned at two different locations. The thicker film (0.15mL SU-8) shows a significant reduction of roughness; the corner and edge locations exhibit almost 50% and 23% of reduction in the roughness, respectively. The thinner film (0.10mL SU-8) shows a relatively less reduction of roughness; the corner and center locations exhibit almost 9% and 25% of reduction in the roughness, respectively. Although the wrinkles are reduced, both samples show much larger roughness compared to the samples used in the method 1 with a narrow period of 1 mm.

Table 9. Average roughness comparison before- and after- Ag deposition.

SU-8 3025	**Scan location**	**R_a [μm] before Ag deposition**	**R_a [μm] after Ag deposition**
0.15mL	Corner	52.4	26.3
	Edge	34.9	26.8
0.10mL	Corner	32.2	31.9
	Center	22.1	16.5

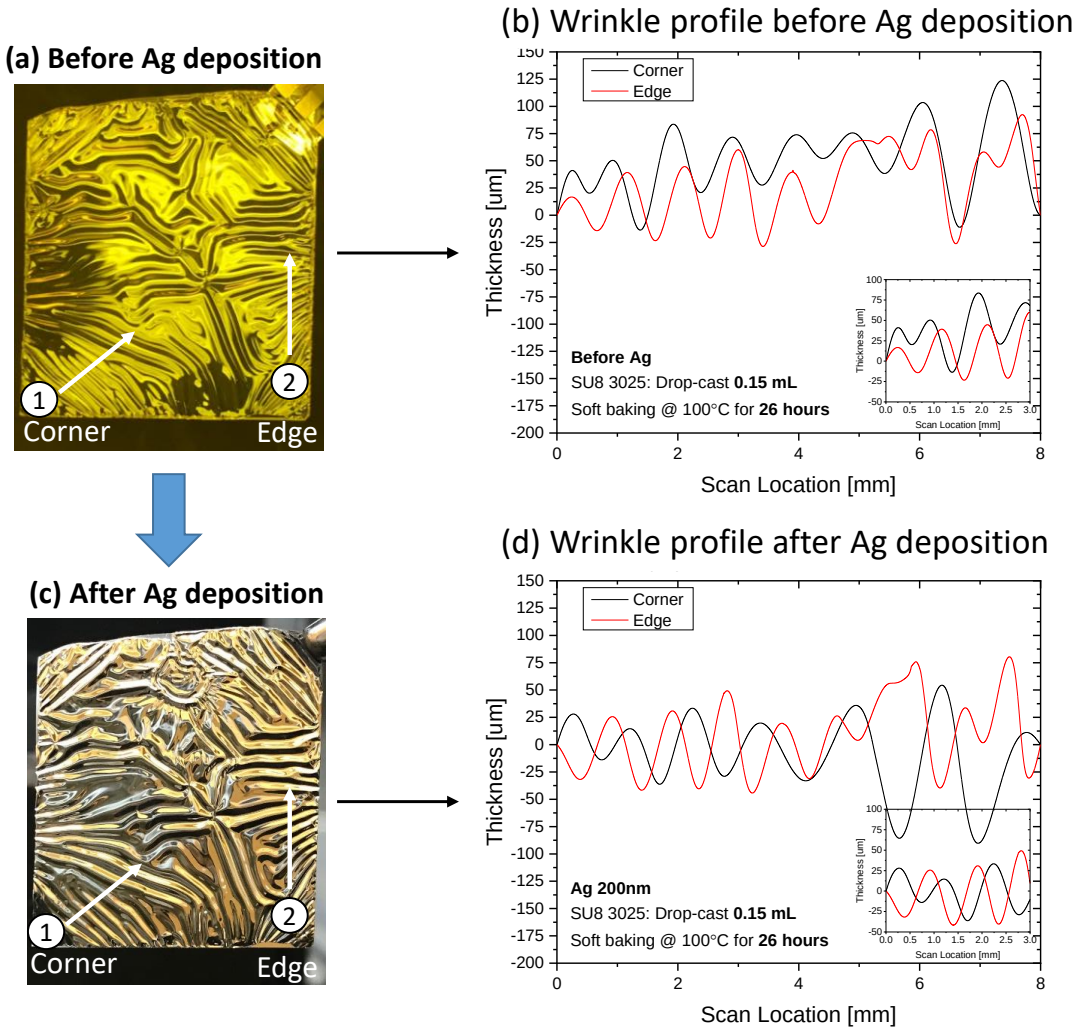

Figure 34. Comparison of wrinkle profiles before- and after- metal deposition for the sample with 0.15mL of SU-8. (a) and (c) are the optical photos of samples before- and after- metal deposition, respectively. (b) and (d) are the wrinkle profile of samples before- and after- metal deposition, respectively.

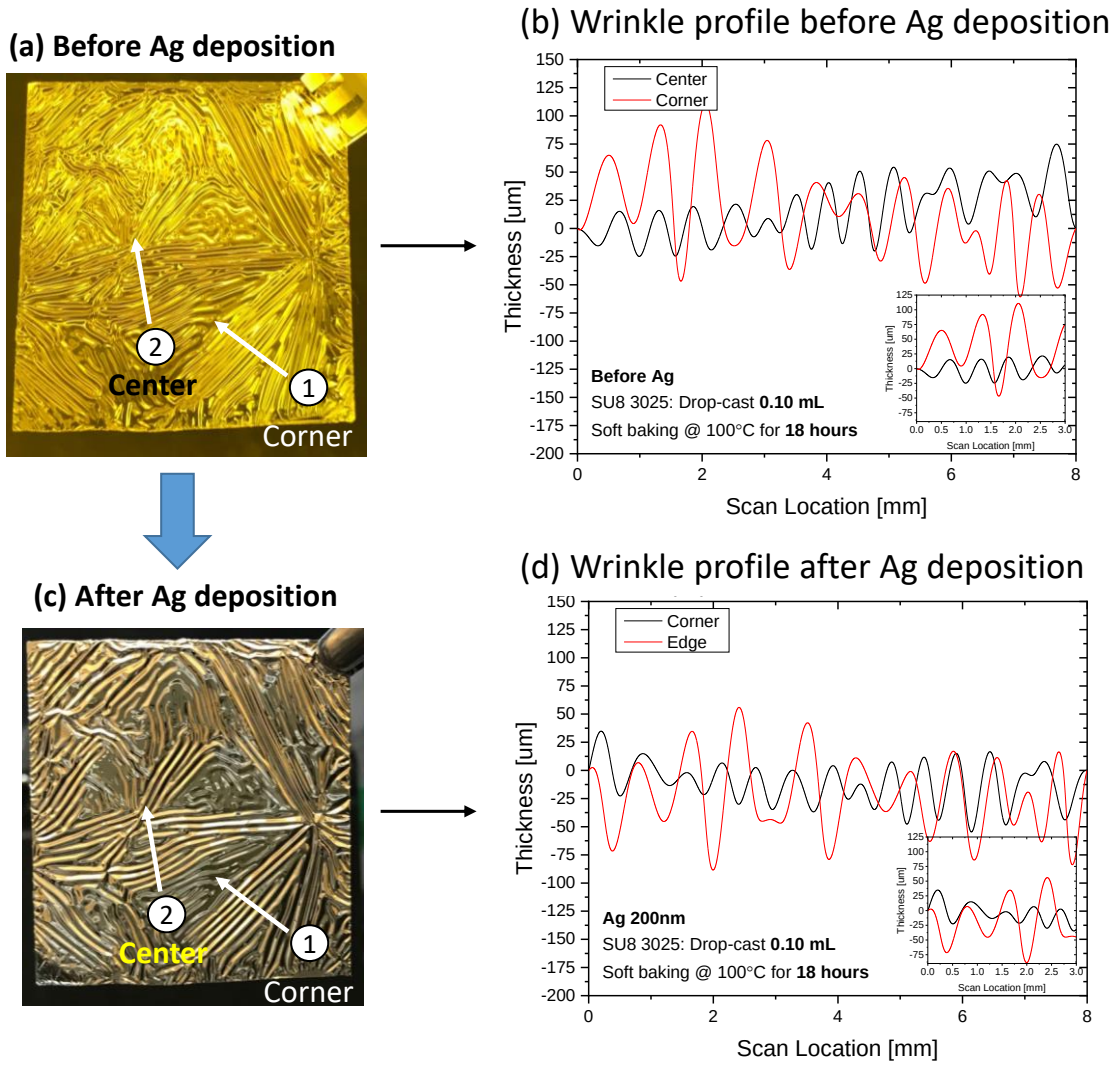

Figure 35. Comparison of wrinkle profiles before- and after- metal deposition for the sample with 0.10mL of SU-8. (a) and (c) are the optical photos of samples before- and after- metal deposition, respectively. (b) and (d) are the wrinkle profile of samples before- and after- metal deposition, respectively.

Chapter 4

CONCLUSION AND FUTURE WORK

In this research, I have investigated optimization of the organic solar cell fabrication by tuning a charge carrier transport layer on an inverted organic solar cell and developing a new metallization method. In focusing on the hole transport layer, MoO_3, an optimized thickness can be determined to produce high power conversion efficiencies by controlling the thickness via thermal deposition in a high vacuum. Results showed that as the layer thickness of MoO_3 reduces, the power conversion efficiency increases. In opposition, as the layer thickness of MoO_3 increases, the PCE decreases. This was demonstrated where the power conversion efficiency decreased by 16% as the layer thickness of MoO_3 increased from 15 nm to 25 nm. By optimizing this hole transport layer thickness, highly efficient organic solar cells can be realized based on the inverted device structure. A new metallization technique has also been investigated to replace vacuum deposited silver electrode with electroplated copper, which is less expensive and better fits to the industry manufacturing. This technique demonstrated plating 200 nm of copper on two devices with different thicknesses of the top silver electrode: 30 nm and 150 nm. The device with 30 nm of silver resulted an improved 25% increase in efficiency due to the significant increase of the fill factor, which improved by 35%. This improvement is attributed to the increased top electrode thickness, thereby increasing the conductance of the top electrode significantly while plating an existing thick Ag electrode (150 nm) did not improve since 150 nm of Ag already provides highly conductive current path for hole collection. Although the copper plating solution can potentially reduce the current density by 6.5%, this work has demonstrated improved performances of an inverted OPV by plating by plating 200 nm of Cu on top of 30 nm of Ag. I found that the addition of the Cu electrode to the existing thick Ag electrode (150 nm) did not improve the fill factor since

150 nm of Ag already provides highly conductive current path for hole collection. I also investigated numerous methods to fabricate an optimum wrinkle structure that can be used as a light trapping vehicle for organic solar cells. To generate wrinkles, three different methods were demonstrated with an SU-8 polymer by controlling the SU-8 softness: (1) generating wrinkles on thin SU-8 after metal deposition, (2) generating wrinkles on a thick SU-8 after metal deposition, and (3) generating wrinkles on a thick SU-8 before metal deposition. Method (1) showed how different metals (Al, Cr, and Cu), thermally evaporated on top of SU-8 in a high vacuum chamber, can generate different wrinkle profiles due their thermal expansion coefficients. For Al, surface roughness decreases as SU-8 film becomes thinner. For Cr, surface roughness resulted in cracks as the difference of thermal expansion coefficients of Cr/SU-8 was significantly much larger than that of Al/SU-8. For Cu, more experiments are needed to validate a consistent trend of surface roughness. Method (2) utilized a thicker SU-8, done by drop-casting and followed by silver deposition. As time increased, it was found that deep within SU-8 was still soft against the outer hard, metal surface. This promoted wrinkles as the silver metal layer needed to accommodate the soft SU-8, where the solvent inside the SU-8 still needed to evaporate. Although results showed improvement of the wrinkle structure, the period of about 3 mm is too large for light trapping to be effective for an organic solar cell. Thus, Method (3) was performed, where a thicker SU-8 film was drop-casted and wrinkles were generated before metal deposition. Thicknesses of 0.10 mL and 0.15 mL SU-8 3025 was drop-casted and allowed annealing on the hot plate, in addition to cooling time (the sample sets at room temperature after taken off the hotplate). This method required an increased amount of annealing time for the SU-8 polymer to evaporate. The annealing time ranged from 12 hours to 26 hours, which was incredibly too long to process. This method demonstrated how time could vary from hours and days, to possibly months when generating

wrinkles. However, I found that this method provides a more suitable wrinkle profile since it shows a significant improvement. The process will not be easily reproducible since it requires prolonged process time to fabricate the wrinkles. However, the outcome of the last method encourages future work to be completed for organic solar cell applications.

With an optimized process, a solar cell can be fabricated on top of the wrinkle structure, enhancing light trapping, thus power conversion efficiency. In addition, the wrinkles direct more sunlight with obligation incident angles back into the active layer of the solar cell, hence, improving light absorption as well. Therefore, my future work will focus on the development of reproducible, scalable, and high throughput wrinkle fabrication with an optimum profile and the demonstration of highly efficient organic solar cells by enhancing light trapping thanks to the wrinkles.

REFERENCES

[1] U.S. Energy Information Administration (EIA). (2018). *Total Energy*. Available: https://www.eia.gov/totalenergy/data/monthly/pdf/mer.pdf

[2] U.S. Naval Research Laboratory (NRL). *Vanguard Project*. Available: https://www.nrl.navy.mil/accomplishments/rockets/vanguard-project/

[3] Solar Impulse Foundation. (2016). *Historic Flight*. Available: https://aroundtheworld.solarimpulse.com/our-story

[4] Solar Server Global Solar Industry Website. (2008). *Waldopolenz Energy Park: Thin-film photovoltaic on the way to the world's biggest solar electric power park*. Available: https://www.solarserver.com/solar-magazine/solar-energy-system-of-the-month/waldpolenz-energy-park.html

[5] Lifewire. (2018). *The 8 Best Portable Solar Chargers to Buy in 2018*. Available: https://www.lifewire.com/best-portable-solar-chargers-4149830

[6] Z. Wang, E. Wang, L. Hou, F. Zhang, M. R. Andersson, and O. Inganäs, "Mixed solvents for reproducible photovoltaic bulk heterojunctions," 2011, vol. 1, p. 8: SPIE.

[7] M.-H. Jao, H.-C. Liao, and W.-F. Su, "Achieving a high fill factor for organic solar cells," *Journal of Materials Chemistry A*, 10.1039/C6TA00126B vol. 4, no. 16, pp. 5784-5801, 2016.

[8] S. J. Kim, G. Y. Margulis, S.-B. Rim, M. L. Brongersma, M. D. McGehee, and P. Peumans, "Geometric light trapping with a V-trap for efficient organic solar cells," *Optics Express*, vol. 21, no. S3, pp. A305-A312, 2013/05/06 2013.

[9] Q.-D. Ou, Y.-Q. Li, and J.-X. Tang, "Light Manipulation in Organic Photovoltaics," *Advanced Science*, vol. 3, no. 7, p. 1600123, 2016.

[10] J. Yoon, K. Kang, S. Kim, and J. Kim, "Effect of oblique incidence angle of sunlight on the optimized folding angle of V-shaped organic solar cells," *Current Applied Physics*, vol. 15, no. 4, pp. 446-451, 2015/04/01/ 2015.

[11] W. Shi Hao *et al.*, "A textured SiO 2 antireflection layer for efficient organic solar cells," *Surface Topography: Metrology and Properties*, vol. 2, no. 3, p. 035005, 2014.

[12] S. Wiesendanger, M. Zilk, T. Pertsch, C. Rockstuhl, and F. Lederer, "Combining randomly textured surfaces and photonic crystals for the photon management in thin film microcrystalline silicon solar cells," *Optics Express*, vol. 21, no. S3, pp. A450-A459, 2013/05/06 2013.

[13] H. A. Atwater and A. Polman, "Plasmonics for improved photovoltaic devices," *Nature Materials*, Review Article vol. 9, p. 205, 02/19/online 2010.

[14] B. Liu *et al.*, "Broadband light trapping based on periodically textured ZnO thin films," *Nanoscale*, 10.1039/C5NR01528F vol. 7, no. 21, pp. 9816-9824, 2015.

[15] K. Tvingstedt, S. D. Zilio, O. Inganäs, and M. Tormen, "Trapping light with micro lenses in thin film organic photovoltaic cells," *Optics Express*, vol. 16, no. 26, pp. 21608-21615, 2008/12/22 2008.

[16] W. Cao and J. Xue, "Recent progress in organic photovoltaics: device architecture and optical design," *Energy & Environmental Science*, 10.1039/C4EE00260A vol. 7, no. 7, pp. 2123-2144, 2014.

[17] M. Burresi, F. Pratesi, F. Riboli, and D. S. Wiersma, "Complex Photonic Structures for Light Harvesting," *Advanced Optical Materials*, vol. 3, no. 6, pp. 722-743, 2015.

[18] C. Trompoukis *et al.*, "Photonic nanostructures for advanced light trapping in thin crystalline silicon solar cells," *physica status solidi (a)*, vol. 212, no. 1, pp. 140-155, 2015.
[19] A. Luque and S. Hegedus, "Handbook of Photovoltaic Science and Engineering (2nd Edition)," ed: John Wiley & Sons.
[20] K. Tvingstedt, V. Andersson, F. Zhang, and O. Inganas, "Folded reflective tandem polymer solar cell doubles efficiency," *Applied Physics Letters*, vol. 91, no. 12, p. 123514, 2007.
[21] S.-B. Rim, S. Zhao, S. R. Scully, M. D. McGehee, and P. Peumans, "An effective light trapping configuration for thin-film solar cells," *Applied Physics Letters*, vol. 91, no. 24, p. 243501, 2007/12/10 2007.
[22] Y. Zhou, F. Zhang, K. Tvingstedt, W. Tian, and O. Inganäs, "Multifolded polymer solar cells on flexible substrates," *Applied Physics Letters*, vol. 93, no. 3, p. 033302, 2008/07/21 2008.
[23] H. Zhen *et al.*, "Inverted indium-tin-oxide-free cone-shaped polymer solar cells for light trapping," *Applied Physics Letters*, vol. 100, no. 21, p. 213901, 2012/05/21 2012.
[24] C. Cho *et al.*, "Random and V-groove texturing for efficient light trapping in organic photovoltaic cells," *Solar Energy Materials and Solar Cells*, vol. 115, pp. 36-41, 2013/08/01/ 2013.
[25] C. Cho and J.-Y. Lee, "Multi-scale and angular analysis of ray-optical light trapping schemes in thin-film solar cells: Micro lens array, V-shaped configuration, and double parabolic trapper," *Optics Express*, vol. 21, no. S2, pp. A276-A284, 2013/03/11 2013.
[26] K. Wang, C. Liu, T. Meng, C. Yi, and X. Gong, "Inverted organic photovoltaic cells," *Chemical Society Reviews*, 10.1039/C5CS00831J vol. 45, no. 10, pp. 2937-2975, 2016.
[27] G. Yu, J. Gao, J. C. Hummelen, F. Wudl, and A. J. Heeger, "Polymer Photovoltaic Cells: Enhanced Efficiencies via a Network of Internal Donor-Acceptor Heterojunctions," *Science*, vol. 270, no. 5243, pp. 1789-1791, 1995.
[28] K. W. Wong *et al.*, "Blocking reactions between indium-tin oxide and poly (3,4-ethylene dioxythiophene):poly(styrene sulphonate) with a self-assembly monolayer," *Applied Physics Letters*, vol. 80, no. 15, pp. 2788-2790, 2002/04/15 2002.
[29] M. P. de Jong, L. J. van Ijzendoorn, and M. J. A. de Voigt, "Stability of the interface between indium-tin-oxide and poly(3,4-ethylenedioxythiophene)/poly(styrenesulfonate) in polymer light-emitting diodes," *Applied Physics Letters*, vol. 77, no. 14, pp. 2255-2257, 2000/10/02 2000.
[30] M. T. Lloyd *et al.*, "Influence of the hole-transport layer on the initial behavior and lifetime of inverted organic photovoltaics," *Solar Energy Materials and Solar Cells*, vol. 95, no. 5, pp. 1382-1388, 2011/05/01/ 2011.
[31] M. T. Lloyd *et al.*, "Impact of contact evolution on the shelf life of organic solar cells," *Journal of Materials Chemistry*, 10.1039/B910213B vol. 19, no. 41, pp. 7638-7642, 2009.
[32] L.-M. Chen, Z. Hong, G. Li, and Y. Yang, "Recent Progress in Polymer Solar Cells: Manipulation of Polymer:Fullerene Morphology and the Formation of Efficient Inverted Polymer Solar Cells," *Advanced Materials*, vol. 21, no. 14-15, pp. 1434-1449, 2009/04/20 2009.
[33] F. C. Krebs, "Air stable polymer photovoltaics based on a process free from vacuum steps and fullerenes," *Solar Energy Materials and Solar Cells*, vol. 92, no. 7, pp. 715-726, 2008/07/01/ 2008.

[34] Z. Xu *et al.*, "Vertical Phase Separation in Poly(3-hexylthiophene): Fullerene Derivative Blends and its Advantage for Inverted Structure Solar Cells," *Advanced Functional Materials,* vol. 19, no. 8, pp. 1227-1234, 2009/04/23 2009.
[35] H.-L. Yip and A. K. Y. Jen, "Recent advances in solution-processed interfacial materials for efficient and stable polymer solar cells," *Energy & Environmental Science,* 10.1039/C2EE02806A vol. 5, no. 3, pp. 5994-6011, 2012.
[36] N. Ahmad, J. Stokes, N. A. Fox, M. Teng, and M. J. Cryan, "Ultra-thin metal films for enhanced solar absorption," *Nano Energy,* vol. 1, no. 6, pp. 777-782, 2012/11/01/ 2012.
[37] M. S. Kumar and K. Balachander, "Performance analysis of different top metal electrodes in inverted polymer solar cells," *Optik - International Journal for Light and Electron Optics,* vol. 127, no. 5, pp. 2725-2731, 2016/03/01/ 2016.
[38] C.-M. Lee and J. Choi, "Polarization and incidence angle-dependent transmittance of transparent nickel electrodes with various thicknesses," *Optical Materials,* vol. 33, no. 6, pp. 859-864, 2011/04/01/ 2011.
[39] X. Fan, J. Wang, H. Wang, X. Liu, and H. Wang, "Bendable ITO-free Organic Solar Cells with Highly Conductive and Flexible PEDOT:PSS Electrodes on Plastic Substrates," *ACS Applied Materials & Interfaces,* vol. 7, no. 30, pp. 16287-16295, 2015/08/05 2015.
[40] A. Lennon, Y. Yao, and S. Wenham, "Evolution of metal plating for silicon solar cell metallisation," *Progress in Photovoltaics: Research and Applications,* vol. 21, no. 7, pp. 1454-1468, 2013/11/01 2012.
[41] S. Aksu, S. Pethe, A. Kleiman-Shwarsctein, S. Kundu, and M. Pinarbasi, "Recent advances in electroplating based CIGS solar cell fabrication," in *2012 38th IEEE Photovoltaic Specialists Conference,* 2012, pp. 003092-003097.
[42] A. Rehman and S. Lee, "Review of the Potential of the Ni/Cu Plating Technique for Crystalline Silicon Solar Cells," *Materials,* vol. 7, no. 2, p. 1318, 2014.
[43] S. Choi, W. J. Potscavage, and B. Kippelen, "Area-scaling of organic solar cells," *Journal of Applied Physics,* vol. 106, no. 5, p. 054507, 2009/09/01 2009.
[44] Y. Zhou *et al.*, "A Universal Method to Produce Low–Work Function Electrodes for Organic Electronics," *Science,* 10.1126/science.1218829 vol. 336, no. 6079, p. 327, 2012.
[45] Y.-C. Chen and A. J. Crosby, "Wrinkling of inhomogeneously strained thin polymer films," *Soft Matter,* 10.1039/C2SM26822A vol. 9, no. 1, pp. 43-47, 2013.
[46] J. Moon *et al.*, "Organic wrinkles for energy efficient organic light emitting diodes," *Organic Electronics,* vol. 26, pp. 273-278, 2015/11/01/ 2015.
[47] X. Fan, B. Xu, S. Liu, C. Cui, J. Wang, and F. Yan, "Transfer-Printed PEDOT:PSS Electrodes Using Mild Acids for High Conductivity and Improved Stability with Application to Flexible Organic Solar Cells," *ACS Applied Materials & Interfaces,* vol. 8, no. 22, pp. 14029-14036, 2016/06/08 2016.
[48] J. S. Choi, Y. Piao, and T. S. Seo, "Generation of hierarchical nano- and microwrinkle structure for smooth muscle cell alignment," *Biotechnology and Bioprocess Engineering,* journal article vol. 19, no. 2, pp. 269-275, March 01 2014.
[49] Z.-J. Zhao, X. Li, and S.-H. Park, "Generation of various wrinkle shapes on single surface by controlling thickness of weakly polymerized layer," *Materials Letters,* vol. 155, pp. 125-129, 2015/09/15/ 2015.
[50] R. Huang, C. M. Stafford, and B. D. Vogt, "Wrinkling of Ultrathin Polymer Films," *MRS Proceedings,* vol. 924, pp. 0924-Z04-10, 2006, Art. no. 0924-z04-10.

[51] S. Chung, J. H. Lee, M.-W. Moon, J. Han, and R. D. Kamm, "Non-Lithographic Wrinkle Nanochannels for Protein Preconcentration," *Advanced Materials,* vol. 20, no. 16, pp. 3011-3016, 2008/08/18 2008.
[52] D. Yan, K. Zhang, F. Peng, and G. Hu, "Tailoring the wrinkle pattern of a microstructured membrane," *Applied Physics Letters,* vol. 105, no. 7, p. 071905, 2014/08/18 2014.
[53] C.-M. Chen, J. C. Reed, and S. Yang, "Guided wrinkling in swollen, pre-patterned photoresist thin films with a crosslinking gradient," *Soft Matter,* 10.1039/C3SM51881G vol. 9, no. 46, pp. 11007-11013, 2013.
[54] N. Bowden, S. Brittain, A. G. Evans, J. W. Hutchinson, and G. M. Whitesides, "Spontaneous formation of ordered structures in thin films of metals supported on an elastomeric polymer," *Nature,* vol. 393, p. 146, 05/14/online 1998.
[55] S. S. Yoo *et al.*, "Cumulative energy analysis of thermally-induced surface wrinkling of heterogeneously multilayered thin films," *Soft Matter,* 10.1039/C7SM02027A vol. 14, no. 5, pp. 704-710, 2018.
[56] C. Steinberg, M. Belgouzi, K. Dhima, M. Papenheim, S. Wang, and H.-C. Scheer, "Thermal wrinkling of nanoimprinted SU-8 with masked UV-exposure," *Journal of Vacuum Science & Technology B,* vol. 33, no. 6, p. 06F603, 2015/11/01 2015.
[57] P.-P. Cheng, L. Zhou, J.-A. Li, Y.-Q. Li, S.-T. Lee, and J.-X. Tang, "Light trapping enhancement of inverted polymer solar cells with a nanostructured scattering rear electrode," *Organic Electronics,* vol. 14, no. 9, pp. 2158-2163, 2013/09/01/ 2013.
[58] J. Yun *et al.*, "Light trapping in bendable organic solar cells using silica nanoparticle arrays," *Energy & Environmental Science,* 10.1039/C4EE01100G vol. 8, no. 3, pp. 932-940, 2015.
[59] J. A. Mayer, B. Gallinet, T. Offermans, I. Zhurminsky, and R. Ferrini, "Self-contained optical enhancement film for printed photovoltaics," *Solar Energy Materials and Solar Cells,* vol. 163, pp. 51-57, 2017/04/01/ 2017.
[60] C. Teck Kong, W. Jonathan, M. Sudha, and R. C. Kylie, "Optimal wavelength scale diffraction gratings for light trapping in solar cells," *Journal of Optics,* vol. 14, no. 2, p. 024012, 2012.
[61] Y.-G. Bi *et al.*, "Dual-periodic-corrugation-induced broadband light absorption enhancement in organic solar cells," *Organic Electronics,* vol. 27, pp. 167-172, 2015/12/01/ 2015.
[62] R. Lampande, G. W. Kim, M. J. Park, B. Y. Kang, and J. H. Kwon, "Efficient light harvesting in inverted polymer solar cells using polymeric 2D-microstructures," *Solar Energy Materials and Solar Cells,* vol. 151, pp. 162-168, 2016/07/01/ 2016.
[63] L. McMillon-Brown *et al.*, "Light-trapping in polymer solar cells by processing with nanostructured diatomaceous earth," *Organic Electronics,* vol. 51, pp. 422-427, 2017/12/01/ 2017.
[64] J. B. Kim *et al.*, "Wrinkles and deep folds as photonic structures in photovoltaics," *Nature Photonics,* Article vol. 6, p. 327, 04/22/online 2012.
[65] J.-J. Fang, H.-W. Tsai, I. C. Ni, S.-D. Tzeng, and M.-H. Chen, "The formation of interfacial wrinkles at the metal contacts on organic thin films," *Thin Solid Films,* vol. 556, pp. 294-299, 2014/04/01/ 2014.
[66] Microchem, "SU-8 3000 Permanent Epoxy Negative Photoresist," in *SU-8 3000 Data Sheet,* 4.2 ed.